Entanglement dynamics of detectors in an Einstein cylinder

Shih-Yuin Lin,[a,b,c] **Chung-Hsien Chou**[d] **and B.L. Hu**[e]

[a] *Department of Physics, National Changhua University of Education,*
  Changhua 50007, Taiwan
[b] *Department of Physics and Astronomy, University of Waterloo,*
  Waterloo, Ontario N2L 3G1, Canada
[c] *Perimeter Institute for Theoretical Physics,*
  Waterloo, Ontario N2L 2Y5, Canada
[d] *Department of Physics, National Cheng Kung University,*
  Tainan 70101, Taiwan
[e] *Maryland Center for Fundamental Physics and Joint Quantum Institute, University of Maryland,*
  College Park, Maryland 20742-4111, U.S.A.

  E-mail: sylin@cc.ncue.edu.tw, chouch@mail.ncku.edu.tw, blhu@umd.edu

ABSTRACT: We investigate how nontrivial topology affects the entanglement dynamics between a detector and a quantum field and between two detectors mediated by a quantum field. Nontrivial topology refers to both that of the *base space* and that of the *bundle*. Using a derivative-coupling Unruh-DeWitt-like detector model interacting with a quantum scalar field in an Einstein cylinder $\mathbf{S}^1$ (space) $\times \mathbf{R}_1$ (time), we see the beating behaviors in the dynamics of the detector-field entanglement and the detector-detector entanglement, which distinguish from the results in the non-compact (1+1) dimensional Minkowski space. The beat patterns of entanglement dynamics in a normal and a twisted field with the same parameter values are different because of the difference in the spectrum of the field modes. In terms of the kinetic momentum of the detectors, we find that the contribution by the zero mode in a normal field to entanglement dynamics has no qualitative difference from those by the nonzero modes.

Contents

1 Introduction

The last decade has seen a rapid increase of research in relativistic quantum information (RQI) (see, e.g., [1]), which studies the relativistic features of quantum information with "relativistic" referring to the *localized quantum objects in relativistic motion*, the *relativistic nature of quantum fields* and the *properties of spacetime structures*. In particular, the

third aspect concerning spacetime properties ranges from the rudimentary yet necessary, such as time-dilation and hypersurface-slicing considerations [2, 3] at the level of special relativity, to spacetime curvature and topology effects [4–6] often considered in the context of general relativity. The present work will focus on how nontrivial topology affects the entanglement dynamics of a system of N (= 1 or 2 here) detectors, which are localized atom-like quantum objects with internal degrees of freedom sensitive to the field they interact with. Here, nontrivial topology refers to the *base space*, turning a flat, noncompact two dimensional Minkowski spacetime $\mathbf{R}_1^1 = \mathbf{R}^1$ (space) $\times \mathbf{R}_1$ (time) into a spatially-compact $\mathbf{S}^1$ (space) $\times \mathbf{R}_1$ (time), and also the *bundle*, whose fibre is the range of the field and a field configuration is a cross section — we are interested in seeing how entanglement dynamics for a *twisted field* is different from a normal (untwisted) field.

Before proceeding further we hasten to point out that although the mathematical nature of these investigations is obvious, they are physically relevant to actual experimental setups: boundary effects pertain to the effects of a mirror or a dielectric slab [7] on entanglement, while a $\mathbf{S}^1$ spatial topology refers to a toroidal cavity [8], both are obviously essential components in quantum experiments. On the theoretical side, quantum field theory in spacetimes with boundaries or with nontrivial topology was investigated in the late 70s by Isham, Dowker, DeWitt, and co-workers [9–12]. The prototype spacetime $\mathbf{S}^1 \times \mathbf{R}_1$ was referred to as the Einstein cylinder (presumably inspired by the "Einstein Universe" with topology $\mathbf{S}^3 \times \mathbf{R}_1$, a static closed Robertson-Walker Universe). The new aspect in our present investigation is entanglement dynamics in this topologically nontrivial spacetime [13], for both untwisted and twisted quantum fields.[1]

Let us ponder upon how the overall features of entanglement dynamics between detectors and fields or between two detectors in a common field would be modified in a circle (e.g., a narrow micro-toroidal cavity) as compared to a straight line, as investigated before in e.g., [17].

Topology of the base space. In $\mathbf{R}^1$ space, dynamics of the detector-field or detector-detector entanglement shows no periodicity at large time scales, we expect entanglement would just grow or decay and saturate. In $\mathbf{S}^1$, the space is finite and compact, so the retarded field emitted by the detector will after one period around the circle return to affect the detector and do so periodically. In a fully enclosed space there is no true dissipation, only apparent one on a time scale short compared to the recurrence time, as well illustrated in the Kac ring [18], a 1D closed harmonic chain, but the energy apparently "lost" to the rest of the chain will be replenished after one period.[2] This of course is the advantage for information processing using micro-toroidal cavities (the space in realistic situations is of course not fully enclosed, as there will be input and output laser activities). For quantum systems the time lag between successive cycles generates interference which shows up as beats. Unlike in $\mathbf{R}^1$, where equilibrium or steady state can be found to exist at late times, in $\mathbf{S}^1$, beating in entanglement distinguishes its behavior.

---

[1]The effect of the topology of the *state-vector space* on the decoherence and entanglement processes has been investigated for some time. See, e.g., [14–16].

[2]Entanglement propagation in a quantum Kac ring has been studied by [19].

Topology of the bundle. Here the nontrivial topology exists in twisted fields, thus the comparison we aim at is between the entanglement dynamics of normal (untwisted) and twisted fields. In $\mathbf{S}^1$, the untwisted and twisted fields possess different eigen-modes, and hence different beat patterns. The normal field possesses a zero mode whereas for twisted fields there is no zero-mode. Note that the existence of the zero mode is a topological, not a geometric effect, in the sense that for normal fields different sizes of $\mathbf{S}^1$ as in a toroidal cavity will all possess a zero mode. Likewise there is no zero mode for twisted fields for all sizes of $\mathbf{S}^1$ cavity.

We mention two related work [4, 5, 13] which uses the time-dependent perturbation theory with a switching function type of interaction to study the finite-time response of a single 2-level Unruh-DeWitt detector and the quantum entanglement of two such detectors [13] in locally flat (3+1) dimensional spacetimes with different topologies. The lowest-order results do depend on the field spectrum, which in turn depend on the spatial topology, though the differences in different topologies are small. However, their lowest-order results do not show beating behavior. The main reason is that the influences by the echoes of a detector itself, as well as the retarded influences by the other detectors separated at a distance, arise from the higher order terms in the coupling expansion.

Below, we use a nonperturbative method to study the nonequilibrium dynamics of a harmonic-oscillator detector-field system with all the mutual influences included in our consideration, in order to capture the full extent of the topological effect in entanglement dynamics. The setup in our study is introduced in section 2. We consider a Unruh-DeWitt-like (UD') detector theory with derivative-coupling [20–25] because a usual detector minimally coupled to a scalar field in (1+1) dimensional Minkowski space has undesirable non-positive-definite energy and higher-derivative radiation-reaction.[3] In section 3 we consider one detector interacting with a quantum field in an Einstein cylinder and compare its entanglement behavior with earlier results obtained for Minkowski space $\mathbf{R}_1^1$. In section 4 we consider the entanglement dynamics of two identical UD' detectors in the presence of a quantum field in the same $\mathbf{S}^1 \times \mathbf{R}_1$ spacetime for both normal and twisted fields. Our findings are summarized in section 5. More details about the two-point correlators of a UD' detector in $\mathbf{R}_1^1$ are presented in appendix A. In our numerical results, we set $c = \hbar = 1$.

2 Model

Consider a (1+1) dimensional flat spacetime with topology $\mathbf{S}^1$ in space and $\mathbf{R}_1$ in time, namely, the Einstein cylinder. The metric is given by

$$ds^2 = -dt^2 + dx^2, \tag{2.1}$$

where $x = R\varphi$ with radius R a positive real constant and the azimuthal angle $\varphi \in (-\pi, \pi]$. The circumference of the circle is thus $L \equiv 2\pi R$. We will also refer to the extended space $x, x' \in \mathbf{R}^1$ obtained by identifying the points x to x mod L (see figure 1). Consider placing

---

[3]An additional advantage when using time-dependent perturbation theory is that the infrared behavior of the response function of a detector with derivative-coupling is better than that with minimal-coupling in (1+1) dimensions, see [26].
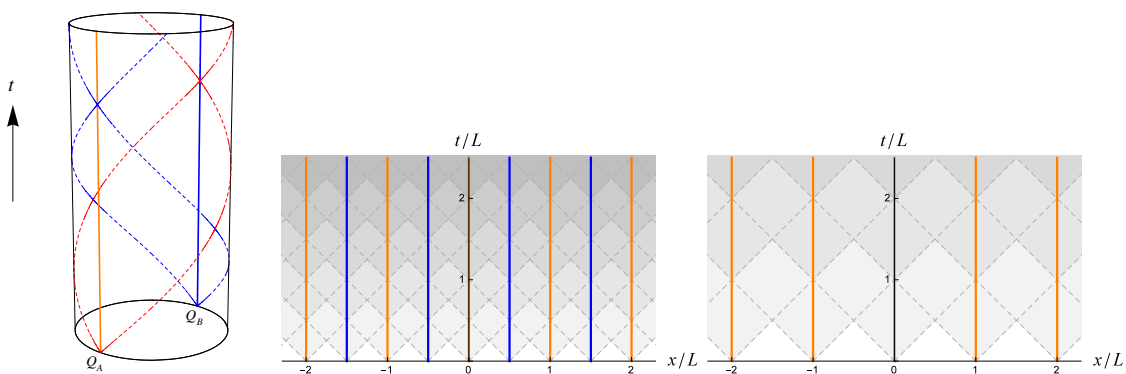
Figure 1. (Left) The setup. The harmonic oscillators Q_A and Q_B are the internal degrees of freedom of detectors A and B located at $x = 0$ and $x = L/2 \equiv R\pi$, respectively. At $t = 0$ we let the UD' detectors begin to couple with the field. The orange and blue solid lines are the worldlines of the two detectors, and the dashed lines represent the fronts of the retarded influences sourced by the detectors after the interaction is switched on. (Middle) An equivalent setup in the extended coordinates in space $\mathbf{R}^1$ by identifying the points x to $x \bmod L$. (Right) Similar diagram for the cases with a single detector Q_A only.

a finite number of the derivative-coupling Unruh-DeWitt-like (UD') [20–23, 25] detectors with the internal harmonic oscillators $Q_{\mathbf{d}}$ coupled to a common massless scalar field Φ in the above spacetime, described by the action

$$S = -\frac{1}{2} \int d^2x\, \partial_\alpha \Phi \partial^\alpha \Phi + \sum_{\mathbf{d}} \frac{1}{2} \int d\tau_{\mathbf{d}} \left[(\partial_{\mathbf{d}} Q_{\mathbf{d}})^2 - \omega_{\mathbf{d}}^2 Q_{\mathbf{d}}^2 \right] + S_I \tag{2.2}$$

where the interaction action is

$$S_I = -\sum_{\mathbf{d}} \lambda \int d\tau_{\mathbf{d}} Q_{\mathbf{d}} \partial_{\mathbf{d}} \int d^2x\, \Phi(t,x) \delta^2 \left(x^\alpha - z_{\mathbf{d}}^\alpha(\tau_{\mathbf{d}}) \right), \tag{2.3}$$

with $x^\alpha = (t, x)$, $\alpha = 0, 1$, the detector label $\mathbf{d} = A$ for one-detector case, $\mathbf{d} = A, B$ for two-detector case, and $\partial_{\mathbf{d}} \equiv d/d\tau_{\mathbf{d}}$. $z_{\mathbf{d}}^\alpha(\tau_{\mathbf{d}})$ are the prescribed trajectory of the detector $\mathbf{d}$. The canonical momenta conjugate to $Q_{\mathbf{d}}$ and Φ are

$$P_{\mathbf{d}}(\tau_{\mathbf{d}}) = \frac{\delta S}{\delta \partial_t Q_{\mathbf{d}}(\tau_{\mathbf{d}})} = \partial_{\mathbf{d}} Q_{\mathbf{d}}(\tau_{\mathbf{d}}), \tag{2.4}$$

$$\Pi(t,x) = \frac{\delta S}{\delta \partial_t \Phi(t,x)} = \partial_t \Phi(t,x) - \sum_{\mathbf{d}} \lambda \int d\tau_{\mathbf{d}} Q_{\mathbf{d}}(\tau_{\mathbf{d}}) v_{\mathbf{d}}^0(\tau_{\mathbf{d}}) \delta^2 \left(x^\alpha - z_{\mathbf{d}}^\alpha(\tau_{\mathbf{d}}) \right), \tag{2.5}$$

respectively, where $v_{\mathbf{d}}^0 \equiv \partial_{\mathbf{d}} z_{\mathbf{d}}^0$. Then, after a Legendre transformation, one can write down the Hamiltonian as

$$H(t) = \sum_{\mathbf{d}} \frac{1}{2 v_{\mathbf{d}}^0(t)} \left\{ P_{\mathbf{d}}^2(t) + \omega_{\mathbf{d}}^2 Q_{\mathbf{d}}^2(\tau_{\mathbf{d}}(t)) \right\}$$
$$+ \frac{1}{2} \int dx \left\{ \left[\Pi_x(t) + \sum_{\mathbf{d}} \lambda \int d\tau_{\mathbf{d}} Q_{\mathbf{d}}(\tau_{\mathbf{d}}) v_{\mathbf{d}}^0(\tau_{\mathbf{d}}) \delta^2 \left(x^\alpha - z_{\mathbf{d}}^\alpha(\tau_{\mathbf{d}}) \right) \right]^2 + \left[\partial_x \Phi_x(t) \right]^2 \right\}, \tag{2.6}$$

which is parametrized by the time variable $x^0 = t$ of the observer's frame and defined on the whole time-slice $x \in \mathbf{S}^1$ associated with t.

Alternatively, one may adopt the interaction action

$$S'_I = \sum_{\mathbf{d}} \lambda \int d\tau_{\mathbf{d}} \partial_{\mathbf{d}} Q_{\mathbf{d}} \int d^2 x \Phi(t,x) \delta^2 (x^\alpha - z^\alpha_{\mathbf{d}}(\tau_{\mathbf{d}})) , \qquad (2.7)$$

plus surface terms evaluated at the initial and final moments from (2.3), which gives the same Euler-Lagrange equations for the dynamical variables $Q_{\mathbf{d}}$ and Φ_x. Starting with (2.7), the canonical momenta conjugate to $Q_{\mathbf{d}}$ and Φ become

$$P'_{\mathbf{d}}(\tau_{\mathbf{d}}) = \partial_{\mathbf{d}} Q_{\mathbf{d}}(\tau_{\mathbf{d}}) + \lambda \Phi(z^\alpha_{\mathbf{d}}(\tau_{\mathbf{d}})) , \qquad (2.8)$$

$$\Pi'(t,x) = \partial_t \Phi(t,x) , \qquad (2.9)$$

respectively, and so the Hamiltonian reads

$$H'(t) = \sum_{\mathbf{d}} \frac{1}{2 v^0_{\mathbf{d}}(t)} \left\{ \left[P'_{\mathbf{d}}(t) - \lambda \Phi_{z^1_{\mathbf{d}}(t)}(t) \right]^2 + \omega^2_{\mathbf{d}} Q^2_{\mathbf{d}}(\tau_{\mathbf{d}}(t)) \right\}$$
$$+ \frac{1}{2} \int dx \left\{ \Pi'^2_x(t) + \left[\partial_x \Phi_x(t) \right]^2 \right\} . \qquad (2.10)$$

While the values of the Hamiltonian H' and the momentum $P_{\mathbf{d}} = \dot{Q}_{\mathbf{d}}$ are invariant under a shift $\Phi_x \to \Phi_x + \mathcal{C}$ with a constant $\mathcal{C}$, such a global symmetry is enough to make the value of $P'_{\mathbf{d}} = \dot{Q}_{\mathbf{d}} + \lambda \Phi(z^\alpha_{\mathbf{d}}(\tau_{\mathbf{d}}))$ not "gauge" invariant. Since we are looking at the reduced state of the detectors in this paper, we prefer to work with (2.3) to get rid of some weird dynamical behaviors of $P'_{\mathbf{d}}$ which could be "gauged away" by the surface terms mentioned below (2.7). Later we will see that the two point correlators $\langle \hat{P}'^2_{\mathbf{d}} \rangle$ and the corresponding uncertainty functions will have indefinite growths in time, while $\langle \hat{P}^2_{\mathbf{d}} \rangle$ of the kinetic momentum is well-behaved.

Suppose the combined system of the detectors and the field is initially in a Gaussian state, which could be pure or mixed. Then the quantum state will always be Gaussian in its history because of the linearity of the interaction. A Gaussian state is fully determined by the two-point correlators of the dynamical variables of the combined system, which can be obtained by taking the expectation values of two operators, evolved in the Heisenberg picture, with respect to the initial state (see, e.g., [17]).

The Heisenberg equations of motion for the operators read

$$\partial^2_{\mathbf{d}} \hat{Q}_{\mathbf{d}}(\tau_{\mathbf{d}}) + \omega^2_{\mathbf{d}} \hat{Q}_{\mathbf{d}}(\tau_{\mathbf{d}}) = -\lambda \partial_{\mathbf{d}} \hat{\Phi}(z_{\mathbf{d}}(\tau_{\mathbf{d}})) , \qquad (2.11)$$

$$-\Box \hat{\Phi}(x) = \lambda \sum_{\mathbf{d}} \int d\tau_{\mathbf{d}} \partial_{\mathbf{d}} \hat{Q}_{\mathbf{d}}(\tau_{\mathbf{d}}) \delta^2 (x^\alpha - z^\alpha_{\mathbf{d}}(\tau_{\mathbf{d}})) , \qquad (2.12)$$

where $\Box \equiv -\partial^2_t + \partial^2_x$. Suppose the detector-field coupling is suddenly switched on at the initial moment $t = 0$ (when $\tau_{\mathbf{d}} \equiv 0$ for all detectors). By virtue of the linearity of the system, the operators will evolve into linear combinations of the operators initially defined

at $t = 0$ as

$$\hat{Q}_{\mathbf{d}}(\tau_{\mathbf{d}}) = \sum_{\mathbf{d}'} \sqrt{\frac{\hbar}{2\omega_{\mathbf{d}}}} \left[q_{\mathbf{d}}^{\mathbf{d}'}(\tau_{\mathbf{d}}) \hat{a}_{\mathbf{d}'} + q_{\mathbf{d}}^{\mathbf{d}'*}(\tau_{\mathbf{d}}) \hat{a}_{\mathbf{d}'}^{\dagger} \right] + \sum_k \sqrt{\frac{\hbar}{2\tilde{\omega}_k}} \left[q_{\mathbf{d}}^k(\tau_{\mathbf{d}}) \hat{b}_k + q_{\mathbf{d}}^{k*}(\tau_{\mathbf{d}}) \hat{b}_k^{\dagger} \right],$$
(2.13)

$$\hat{\Phi}_x(t) = \sum_{\mathbf{d}'} \sqrt{\frac{\hbar}{2\omega_{\mathbf{d}}}} \left[\phi_x^{\mathbf{d}'}(t) \hat{a}_{\mathbf{d}'} + \phi_x^{\mathbf{d}'*}(t) \hat{a}_{\mathbf{d}'}^{\dagger} \right] + \sum_k \sqrt{\frac{\hbar}{2\tilde{\omega}_k}} \left[\phi_x^k(t) \hat{b}_k + \phi_x^{k*}(t) \hat{b}_k^{\dagger} \right], \quad (2.14)$$

with $\tilde{\omega}_k \equiv \omega_k L = |k| L$ for $k \neq 0$ and $\tilde{\omega}_k \equiv 1$ for $k = 0$. Here $q_{\mathbf{d}}^{\mathbf{d}'}$, $q_{\mathbf{d}}^k$, $\phi_x^{\mathbf{d}'}$, and ϕ_x^k are the (c-number) detector-detector, detector-field, field-detector, and field-field mode functions, respectively, $\hat{a}_{\mathbf{d}}$ and $\hat{a}_{\mathbf{d}}^{\dagger}$ are the lowering and raising operators for the free detector $\mathbf{d}$, while $\hat{b}_k$ and $\hat{b}_k^{\dagger}$ are the annihilation and creation operators for the free field mode with wave number k. For the normal (untwisted) field, we take $k = k_n \equiv n/R = 2\pi n/L$, $n \in \mathbf{Z}$ to satisfy the periodic boundary condition $\phi_x^{[0]k_n}(t) = \phi_{x+L}^{[0]k_n}(t)$, and for the twisted field, we take $k = k_n' \equiv [n - (1/2)]/R$, $n \in \mathbf{Z}$ to satisfy the anti-periodic boundary condition $\phi_x^{[0]k_n'}(t) = -\phi_{x+L}^{[0]k_n'}(t)$ (analogous to the Möbius band) [9, 10, 12]. There is one zero mode ($k_0 = 0$ and $\omega_{k_0} = 0$ when $n = 0$) for the untwisted field, and no zero mode for the twisted field. For the zero mode, we define $\hat{b}_0 \equiv (\hat{\Phi}_{k_0} + i\hat{\Pi}_{k_0})/\sqrt{2\hbar}$ with the initial zero-mode field operator and its conjugate momentum operator satisfying the equal-time commutation relation $[\hat{\Phi}_{k_0}, \hat{\Pi}_{k_0}] = i\hbar$.

Since the detectors and the field are free before the detector-field coupling is switched on at $t = \tau_{\mathbf{d}} = 0$, the initial conditions for the mode functions are set to be $\phi_x^k(0) = e^{ikx}$, $\partial_t \phi_x^k(0) = -i\omega_k e^{ikx}$ for $k \neq 0$, $q_{\mathbf{d}}^{\mathbf{d}'}(0) = \delta_{\mathbf{d}}^{\mathbf{d}'}$, $\partial_t q_{\mathbf{d}}^{\mathbf{d}'}(0) = -i\omega_{\mathbf{d}} \delta_{\mathbf{d}}^{\mathbf{d}'}$, and $\phi_x^{\mathbf{d}}(0) = \partial_t \phi_x^{\mathbf{d}}(0) = q_{\mathbf{d}}^k(0) = \partial_t q_{\mathbf{d}}^k(0) = 0$. For the zero-mode component of the free field [27], one has $\hat{\Phi}_{k_0}(t) = \hat{\Phi}_{k_0}(0) + (t/L)\hat{\Pi}_{k_0}(0) = \sqrt{\hbar/2} \left[(1 - (i/L)t)\hat{b}_{k_0} + (1 + (i/L)t)\hat{b}_{k_0}^{\dagger} \right]$, so the initial conditions are set to be $\phi_x^{k_0}(0) = 1$ and $\partial_t \phi_x^{k_0}(0) = -i/L$. The momentum operators conjugate to $\hat{Q}_{\mathbf{d}}$ and $\hat{\Phi}_x$ at $t > 0$ can be obtained straightforwardly by inserting (2.13) and (2.14) to the operator version of (2.4) and (2.5).

In terms of the above expansion, eq. (2.12) yields

$$-\Box \phi_x^{\mu}(t) = \lambda \sum_{\mathbf{d}} \int d\tau_{\mathbf{d}} \partial_{\mathbf{d}} q_{\mathbf{d}}^{\mu}(\tau_{\mathbf{d}}) \delta^2 \left(x^{\alpha} - z_{\mathbf{d}}^{\alpha}(\tau_{\mathbf{d}}) \right)$$
(2.15)

where $\mu = \mathbf{d}, k$, and the mode functions with different μ's are decoupled. Eq. (2.15) implies $\phi_x^{\mu}(t) = \phi_x^{[0]\mu}(t) + \phi_x^{[1]\mu}(t)$, where the homogeneous solutions are $\phi_x^{[0]\mathbf{d}} = 0$, $\phi_x^{[0]k}(t) = e^{-i\omega_k t + ikx}$ for $k \neq 0$, and $\phi_x^{[0]k_0}(t) = 1 - (i/L)t$ for the zero mode, and the inhomogeneous solutions read

$$\phi_x^{[1]\mu}(t) = \sum_{\mathbf{d}} \lambda \int_0^{\infty} d\tau_{\mathbf{d}} G_{\text{ret}} \left(x^{\alpha}; z_{\mathbf{d}}^{\alpha}(\tau_{\mathbf{d}}) \right) \partial_{\mathbf{d}} q_{\mathbf{d}}^{\mu}(\tau_{\mathbf{d}})$$
(2.16)

with the retarded Green's function G_{ret} of the field. When all of the field modes are considered, the retarded Green's function G_{ret} for the massless scalar field can be written as

$$G_{\text{ret}}(t, x; t', x') = \frac{1}{2} \sum_{n \in \mathbf{Z}} \varepsilon^n \theta \left[t + x - (t' + x' + nL) \right] \theta \left[t - x - (t' - x' - nL) \right], \quad (2.17)$$

for $x, x' \in (-L/2, L/2]$. We take $\varepsilon = 1$ for the untwisted field, and $\varepsilon = -1$ for the twisted field. In either case, the retarded Green's function looks the same as the one in Minkowski space around the source point $(t, x) = (t', x')$. One can verify that $-\Box G_{\text{ret}}(t, x; t', x') = \sum_{n \in \mathbf{Z}} \varepsilon^n \delta(t - t') \delta(x - x' - nL)$ in the extended coordinates with $x, x' \in \mathbf{R}^1$ and identifying the points x to x mod L (see figure 1). Now $\phi_x^{[0]\mu}(t)$ can be interpreted as vacuum fluctuations of the field state, while $\phi_x^{[1]\mu}(t)$ behave like the retarded fields sourced by the point-like detectors. Note that, to be consistent with the expressions (2.17), later we have to include the contributions by enough number of the the field modes, namely, the UV cutoff cannot be too small.

For the untwisted field, eq. (2.17) includes the contribution by the zero mode. If we exclude the zero mode entirely, the retarded Green's function for the untwisted field will become [27]

$$
\begin{aligned}
&G_{\text{ret}}^{\text{nz}}(t, x; t', x') \\
&= \lim_{\epsilon \to 0+} \frac{1}{2\pi} \theta(t - t') \operatorname{Im} \left\{ \ln \left(1 - e^{-i(t - t' + (x - x') - i\epsilon)/R} \right) + \ln \left(1 - e^{-i(t - t' - (x - x') - i\epsilon)/R} \right) \right\} \\
&= \frac{1}{2} \sum_{n \in \mathbf{Z}} \theta\big[t + x - (t' + x' + nL) \big] \theta\big[t - x - (t' - x' - nL) \big] - \frac{t - t'}{L} \theta(t - t') . \quad (2.18)
\end{aligned}
$$

Compared with $-\Box G_{\text{ret}}$, here $-\Box G_{\text{ret}}^{\text{nz}}$ has an extra term $-\Box[-(t - t')\theta(t - t')/L] = -(2/L) \delta(t - t')$. This is because the field modes cannot form a complete basis without the zero mode. Moreover, $G_{\text{ret}}^{\text{nz}}$ is nonzero when $|t - t'| < |x - x'|$, which implies that two spacelike separated events located at (t, x) and (t', x') can have superluminal signaling, which violates causality, even at the classical level.

3 One-detector case

Let us start with the simplest case with only one single detector A with natural frequency $\omega_A = \Omega_0$, located at $x = 0$. To study the influence of the quantum field in the $\mathbf{S}^1 \times \mathbf{R}_1$ spacetime on the detector we look at the reduced dynamics of A by tracing out the field. For this purpose we need to calculate the two-point correlators of the detector.

Inserting the solutions of ϕ_x^μ with (2.16) into (2.11), one obtains the equations of motion for the mode functions

$$
(\partial_t^2 + 2\gamma \partial_t + \Omega_0^2) q_A^\mu(t) = -\lambda \partial_t \phi_0^{[0]\mu}(t) - \lambda^2 \sum_{n'=1}^{\infty} \varepsilon^{n'} \theta(t - n'L) \partial_t q_A^\mu(t - n'L) \quad (3.1)
$$

$$
= \begin{cases} -\lambda \partial_t \phi_0^{[0]\mu}(t) & \text{for } t < L \\ \varepsilon(\partial_t^2 - 2\gamma \partial_t + \Omega_0^2) q_A^\mu(t - L) & \text{for } t \geq L , \end{cases} \quad (3.2)
$$

with $\mu = A$, k_n (untwisted field) or k_n' (twisted field), $n \in \mathbf{Z}$, and the coupling strength $\gamma \equiv \lambda^2/4$. When $t \geq L$, the above expressions for different μ's have the same appearance, while the solutions at $0 \leq t < L$ before the first echo hits the detector are generated by different driving forces $\propto \partial_t \phi_0^{[0]\mu}(t)$. Note that the above equations for the twisted field on

$\mathbf{S}^1$ are equivalent to those for a UD' detector in the same scalar field and located at the center of an 1D cavity made of two perfectly-conducting mirrors separated at a distance of L, while the ones for the untwisted field are equivalent to those in a cavity with infinitely-permeable mirrors [7], or in a toroidal cavity [8].

Although the left-hand side (l.h.s.) of (3.1) describes the continuous evolutions of the mode functions, on the right-hand side (r.h.s.) of the equation the influences by the echoes come in a discrete fashion. The analytical solutions for these delayed differential equations can be obtained order by order from those at very early times in principle, but the lengths of the expressions for the solutions grow rapidly as the order of the included echoes increase. Very soon the analytical solutions will get too complicated to read off any useful information. In this case numerical computation would come in handy and give more transparent results.

Below, the delayed differential equations (3.2) will be solved with the proper initial conditions. For $t < L$, the solutions for (3.2) have the closed form

$$q_A^A(t)\big|_{0 \leq t < L} = \frac{e^{-\gamma t}}{2\Omega} \left[\left(\Omega - (\Omega_0 + i\gamma) \right) e^{i\Omega t} + \left(\Omega + (\Omega_0 + i\gamma) \right) e^{-i\Omega t} \right], \qquad (3.3)$$

$$q_A^{k \neq 0}(t)\big|_{0 \leq t < L} = -\lambda \int_0^t d\tau \, \Omega^{-1} K(t - \tau) \partial_t \phi_0^{[0]k}(\tau)$$
$$= \frac{\lambda \omega}{2\Omega} \left(\frac{e^{-i\omega t} - e^{(-\gamma + i\Omega)t}}{\gamma - i(\omega + \Omega)} - \frac{e^{-i\omega t} - e^{(-\gamma - i\Omega)t}}{\gamma - i(\omega - \Omega)} \right), \qquad (3.4)$$

$$q_A^{k_0}(t)\big|_{0 \leq t < L} = -\lambda \int_0^t d\tau \, \Omega^{-1} K(t - \tau) \partial_t \phi_0^{[0]k_0}(\tau)$$
$$= \frac{i\lambda}{\Omega_0^2 L} \left[1 - e^{-\gamma t} \left(\cos \Omega t + \frac{\gamma}{\Omega} \sin \Omega t \right) \right], \qquad (3.5)$$

with $\omega \equiv |k|$ (k can be k_n or k_n'), $\Omega \equiv \sqrt{\Omega_0^2 - \gamma^2}$, and $K(x) \equiv e^{-\gamma x} \sin \Omega x$. The above early-time solutions for $q_A^A(t)$ and $q_A^{k \neq 0}(t)$ are identical to those in Minkowski space [28].

3.1 Eigen-frequencies

3.1.1 Untwisted field

Assume at late times ($t \gg L, 1/\gamma$) the detector would evolve into a stationary state, when the mode function q_A^A could be written as

$$q_A^A(t) \approx \int d\omega \, \tilde{q}_A^A(\omega) e^{i\omega t}. \qquad (3.6)$$

For $\varepsilon = 1$, inserting the above ansatz into (3.1) or (3.2) with $\mu = A$ yields

$$-\omega^2 + \Omega_0^2 = -2\gamma\omega \cot(\omega L/2). \qquad (3.7)$$

The solutions of ω are the eigen-frequencies. One can immediately see that $|\omega| = \Omega_0$ are solutions but only when $R = (1 + 2n)/(2\Omega_0)$ (i.e. $L = \pi(1 + 2n)/\Omega_0$), $n = 0, 1, 2, 3, \ldots$. More general solutions to (3.7) can be obtained by numerical methods. In figure 2 (upper-right)
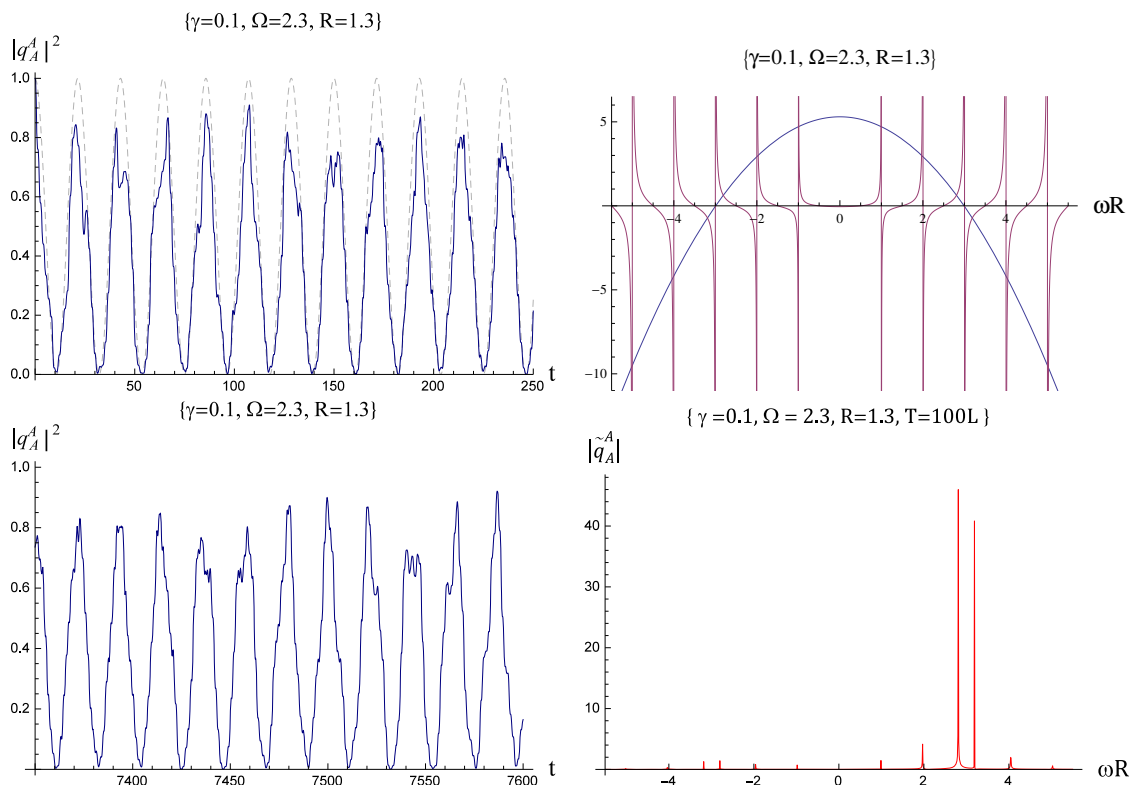
Figure 2. Emergence of the frequency spectrum, after a Fourier transform of q_A^A from $t = 0$ to $t = T \gg L$ (lower-right). In the upper-right plot, the blue and purple curves represent the l.h.s. and r.h.s. of eq. (3.7) as functions of ωR, respectively. Here the l.h.s. $= 0$ at the free detector's natural frequency $\Omega_0 = \pm 2.9928/R \approx 3/R$, where a free-field mode is located. These two frequencies mix together and generate two new eigen-frequencies $\omega R \approx 3.1901$ and 2.8089, which are the closest two among all of the eigen-frequencies in the frequency space. In the lower-right plot one can see that these two eigen-frequencies dominate the long-time behavior of q_A^A, and give the beat of $|q_A^A|^2$ in the left plots. The period of the beat can be estimated from the difference of these two eigen-frequencies: $T_{\text{beat}} \approx 2\pi/(2\Delta) = 2\pi/[(3.1901 - 2.8089)/R] \approx 21.4297$ (the gray dashed curve in the upper-left plot represents $(1 + \cos 2\pi t/T_{\text{beat}})/2 \approx (1 + \cos 2\Delta t)/2$). Compare the upper- and lower-left plots one can see that, while the frequency spectrum gets sharper and sharper as the duration of interaction T increases, the mode function have similar behaviors from early times all the way to late times, if observed in the same small time scale.

one can see that when $\Omega_0 \gg 2\pi/L$, for those $|\omega| < \Omega_0$ ($|\omega| > \Omega_0$), one has $|\omega| < n/R$ ($|\omega| > n/R$), $n = 1, 2, 3, \ldots$.

When $\Omega_0 \approx n/R$ with some positive integer n, while $q_A^{k_n}$ in (3.4) is on resonance at early times (which, together with other modes, produces some resonant oscillation on top of the decaying behavior of the two-point correlators and functions of them, see appendix A), at a larger time scale the detector mode with Ω_0 and the field mode with $\omega_{k_n} = |k_n| = n/R$ will mix together and generate two dominant eigen-modes[4] with frequencies $\omega \approx \Omega_0 \pm \Delta$,

---

[4]In this paper, our "eigen-modes" refer to those $e^{i\omega t}$ in the stationary ansatz for a mode function, e.g., (3.6) or (3.9), rather than the mode function itself. We call the eigen-modes "dominant" if the amplitude $|\tilde{q}(\omega)|$ in the ansatz has the maximum values at the corresponding eigen-frequencies.
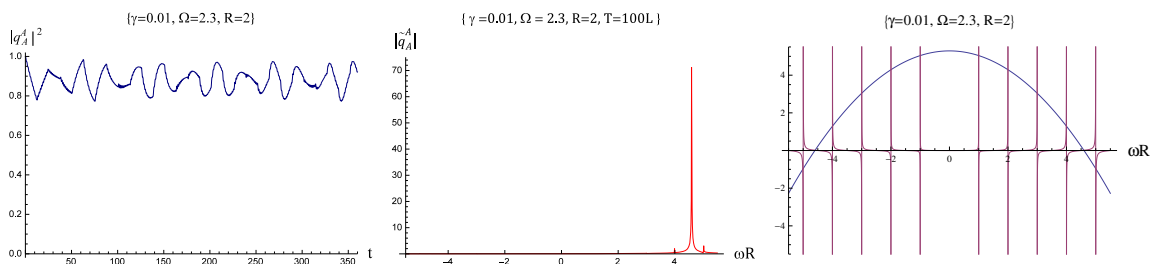
Figure 3. When γ is small and Ω_0 is about $[n - (1/2)]/R$ ($n \in \mathbf{Z}$), which is not close to any n/R, no significant beat can be observed. Here $\gamma = 0.01$, $\Omega = 2.3$, and $R = 2$. The most significant eigen-mode has the frequency closest to Ω_0.

where

$$\Delta \approx \sqrt{\gamma/\pi}\,, \tag{3.8}$$

in the weak coupling limit. These two eigen-modes will dominate the late-time behavior of q_A^A. In particular, the frequency difference produces the beat of $|q_A^A|^2$ at frequency 2Δ, and so $2\pi/(2\Delta) \sim \gamma^{-1/2}$ is the largest significant time scale in the evolution of the single detector system with $\Omega_0 \approx n/R$ in the weak coupling limit. This is very different from the time scale γ^{-1} in the detector theories in Minkowski space.

Even if the radius R or the circumference L of $\mathbf{S}^1$ is larger than the time scale $1/\gamma$, which is the largest time scale of the detector in $(1+1)$ dimensional Minkowski space $\mathbf{R}_1^1$, only the early-time $(0 < t < L)$ behavior of the mode function will be similar to those in $\mathbf{R}_1^1$. Once the echoes start to affect the detector $(t > L)$, the higher-order corrections from the echoes will be the same order of magnitude as the zeroth order solution. At large time scales one can also see the beat feature when $\Omega_0 \approx n/R$ for some integer n.

When Ω_0 is not close to any n/R, $n \in \mathbf{Z}$, the beating behavior may be suppressed. In the example shown in figure 3, when $\Omega_0 \approx [n - (1/2)]/R$ for some n, the only dominant eigen-mode has a frequency very close to Ω_0, and the largest time scale in the evolution of the mode function is about L, which is the period of the massless field traveling over the space $\mathbf{S}^1$. However, if there are more than two dominant modes, the small differences between the frequency-differences of the dominant modes may produce beats at an even larger time scale (e.g., figure 7).

For the detector-field mode function $q_A^{k_n}$, inserting a similar ansatz

$$q_A^{k_n}(t) \approx \int d\omega \tilde{q}_A^{k_n}(\omega)e^{i\omega t} \tag{3.9}$$

into (3.1) or (3.2) with $\mu = k_n$ yields

$$-\omega^2 + \Omega_0^2 = -2\gamma\omega \cot(\omega L/2) - \lambda 2\pi\delta(\omega_{k_n} - \omega)\,. \tag{3.10}$$

The solutions of the eigen-frequencies for $q_A^{k_n}$ are exactly the same as those for q_A^A with the same values of the parameters Ω_0, λ, and L. This is evident when comparing figure 4 with figure 2, and figure 5 with figure 3. One can clearly see the beats in figure 5 while there is no significant beat in figure 3. This is because there are two dominant eigen-modes (with frequencies $\omega \approx \Omega_0$ and $|k_n|$) for $q_A^{k_n}$ in figure 5, rather than one for q_A^A in figure 3.
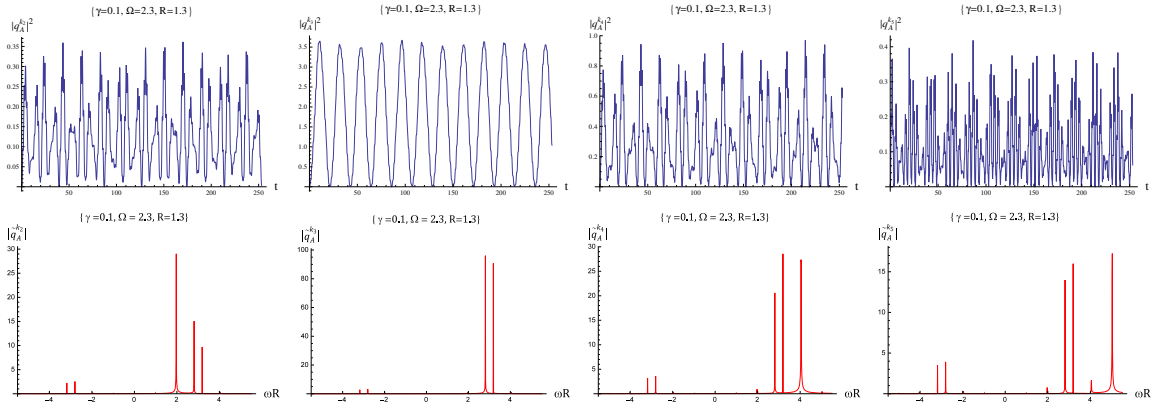
Figure 4. $q_A^{k_n}(t)$ (upper row) and their frequency spectra $\tilde{q}_A^{k_n}(\omega)$ (lower row), $n = 2, 3, 4, 5$ (from left to right), with the same values of the parameters as those in figure 2 ($\gamma = 0.1$, $\Omega = 2.3$, $R = 1.3$). One can see that the eigen-frequencies are exactly the same as those for the q_A^A there.
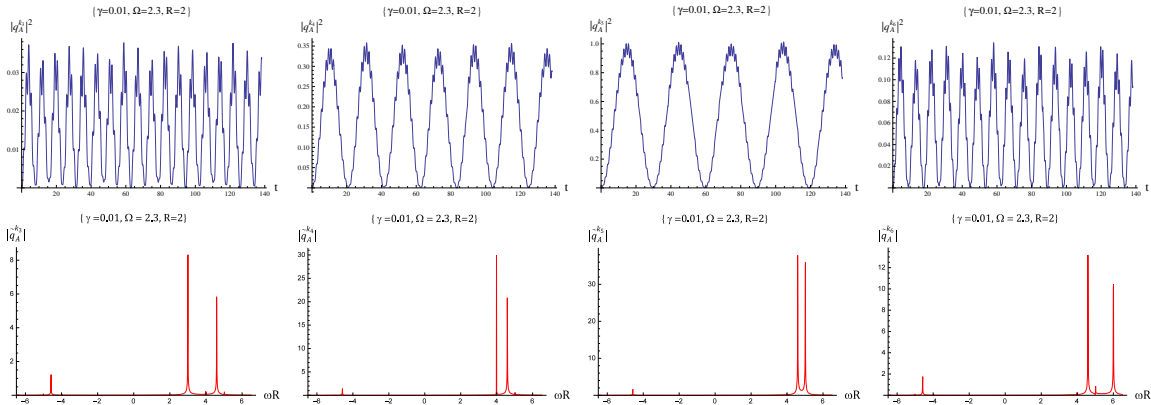

Figure 5. $q_A^{k_n}(t)$ (upper) and their frequency spectra $\tilde{q}_A^{k_n}$ (lower), $n = 3, 4, 5, 6$ (from left to right), with the same parameter values in figure 3 ($\gamma = 0.01$, $\Omega = 2.3$, $R = 2$). The eigen-frequencies are exactly the same as those for the q_A^A there, but now one can see the beats because there are always two dominant eigen-frequencies ($\omega \approx \Omega_0$ and $|k_n|$) for the detector-field mode functions $q_A^{k_n}(t)$.

3.1.2 Twisted field

For $\varepsilon = -1$, inserting ansatz similar to (3.6) or (3.9) into (3.1) or (3.2) yields

$$-\omega^2 + \Omega_0^2 = 2\gamma\omega \tan(\omega L/2)\,, \tag{3.11}$$

$$-\omega^2 + \Omega_0^2 = 2\gamma\omega \tan(\omega L/2) - \lambda 2\pi\delta(\omega_{k'_n} - \omega)\,, \tag{3.12}$$

for $\mu = A$ and $\mu = k'_n$, respectively. Again the eigen-frequencies of $q_A^A(t)$ and $q_A^{k'_n}(t)$ obtained from the above two equations are the same. Since $\tan(\omega L/2) = -\cot(\omega L/2 - \pi/2)$, for ω large enough and not very close to Ω_0, the solutions of (3.11) and (3.12) are roughly those solutions for (3.7) shifted by $\pi/L = 1/(2R)$. (Recall that the modes for the free twisted field have $k'_n = [n - (1/2)]/R$.)

The difference between the spectra of the free fields can alter the beating behavior drastically in different fields while the values of the parameters Ω_0, λ, and L are the same.

For example, for $\Omega_0 \approx n/R$, $n \in \mathbf{Z}$, the beating behavior of $|q_A^A|^2$ is not significant in the twisted field, in contrast to the clear beats in the cases with the same parameter values but in the untwisted field, as those in figure 2. For $\Omega_0 \approx [n - (1/2)]/R$ with large $|n|$, on the other hand, $|q_A^A|^2$ in the twisted field has beats at a frequency about 2Δ with the approximated value of Δ given in (3.8) in the weak coupling limit, while there is no significant beat in the untwisted field with the same parameters, as those in figure 3.

3.2 Two-point correlators and detector-field entanglement

Suppose the initial state of the combined system defined on the $t = 0$ slice is a factorized state,

$$|\psi(0)\rangle = |g\rangle \otimes |0_L\rangle \tag{3.13}$$

which is a product of the ground state of the free detector $|g\rangle$ and the vacuum state of the free field $|0_L\rangle$ in the Einstein cylinder $\mathbf{S}^1 \times \mathbf{R}_1$ [29]. For the untwisted field, the vacuum state is further factorized to $|0_L\rangle = |0_L\rangle_{\mathrm{nz}} \otimes |0_L\rangle_{\mathrm{z}}$, where $|0_L\rangle_{\mathrm{nz}}$ is the lowest energy state of the field with non-zero wave vector, and $|0_L\rangle_{\mathrm{z}}$ is the initial state of the zero mode of the free field, chosen to satisfy $\hat{b}_{k_0}|0_L\rangle_{\mathrm{z}} = 0$, which gives the minimal uncertainty $_{\mathrm{z}}\langle 0_L|(\hat{\Phi}_{k_0}(0))^2|0_L\rangle_{\mathrm{z}} = {}_{\mathrm{z}}\langle 0_L|(\hat{\Pi}_{k_0}(0))^2|0_L\rangle_{\mathrm{z}} = \hbar/2$. For the twisted field there is no zero-mode, thus no similar separation is needed. With the factorized initial state (3.13), the symmetric two-point correlator of the detectors splits into two parts, e.g.,

$$\langle \hat{Q}_A^2(t) \rangle \equiv \langle \hat{Q}_A(t), \hat{Q}_A(t) \rangle \equiv \frac{1}{2} \lim_{t' \to t} \langle \psi(0)|\hat{Q}_A(t)\hat{Q}_A(t') + \hat{Q}_A(t')\hat{Q}_A(t)|\psi(0)\rangle$$
$$= \langle \hat{Q}_A(t), \hat{Q}_A(t) \rangle_{\mathrm{a}} + \langle \hat{Q}_A(t), \hat{Q}_A(t) \rangle_{\mathrm{v}} \tag{3.14}$$

where, from (2.13),

$$\langle \hat{Q}_A(t), \hat{Q}_A(t) \rangle_{\mathrm{a}} = \frac{\hbar}{2\Omega_0} |q_A^A(t)|^2, \tag{3.15}$$

$$\langle \hat{Q}_A(t), \hat{Q}_A(t) \rangle_{\mathrm{v}} = \sum_{n \in \mathbf{Z}} \frac{\hbar}{2\tilde{\omega}_n} |q_A^{k_n}(t)|^2, \tag{3.16}$$

for the untwisted field, and with $k_n \to k_n'$ for the twisted field. The uncertainty $\mathcal{U} \equiv \sqrt{\langle Q_A^2 \rangle \langle P_A^2 \rangle - \langle Q_A, P_A \rangle^2}$ and the purity $\mathcal{P} \equiv Tr(\rho_A^{\mathrm{R}})^2 = 1/(2\mathcal{U})$, where ρ_A^{R} is the reduced state of detector A, will be fully determined by the two-point correlators of the detector since the quantum state of the combined system is always Gaussian in this linear system.

3.2.1 UV cutoff

In appendix A, the symmetric two-point correlators of a UD' detector at rest in $\mathbf{R}_1^1$ with the initial state similar to (3.13) have been worked out. One can see that $\langle Q_A^2 \rangle$, $\langle Q_A, P_A \rangle$, and $\langle P_A^2 \rangle$ all suffer from the UV logarithmic divergence. To control, one has to introduce a UV cutoff ω_M in the integrals (A.6)–(A.9). The values of ω_M cannot be too small, or the uncertainty relation of the detector $\mathcal{U} \geq \hbar/2$ will be violated due to the inconsistency with applying the retarded Green's function in the calculation, similar to the reason we mentioned in section 2.
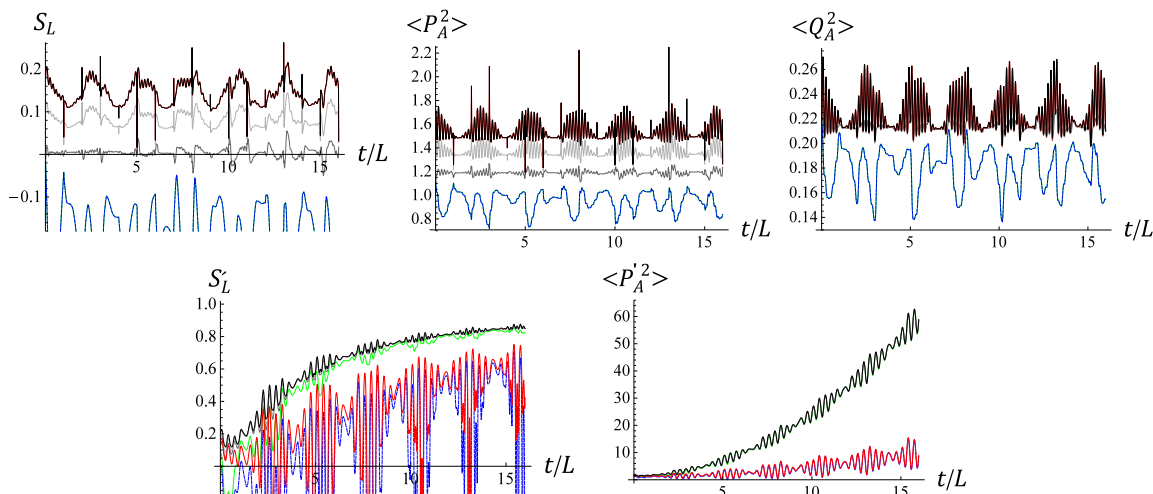
Figure 6. Time-evolutions of the linear entropy S_L, contributed by the correlators $\langle \hat{P}_A^2(t) \rangle$ and $\langle \hat{Q}_A^2(t) \rangle$ (upper row) of single detector A in the untwisted field, with the same parameter values as those in figures 2 and 4. Replacing P_A by the gauge-dependent P_A' defined in (2.8), both $\langle P_A'^2 \rangle$ (lower-right) and the corresponding linear entropy S_L' (lower-left) are always increasing at large time scales. The dark-gray, light-gray, and black curves represent the results contributed by the modes with wave number $k_n = n/R$ from $|n| = 0$ up to $|n| = 10$, 100, and 1000, respectively. One can get a taste of the logarithmic divergence from these three curves, with the magnitudes proportional to $\log n_{\max}$ in the upper-middle plot. The green curves are contributed only by the modes with $n = 0$ and $|n| = 3$, the latter are almost on resonance with the detector. The blue-dashed and red-dotted curves are the green and the black curves with the contributions by the zero mode ($n = 0$) removed, respectively. The difference from those curves with the zero-mode contributions is significant in the lower plots.

How about the correlators for the UD' detector in $\mathbf{S}^1 \times \mathbf{R}_1$?

The logarithmic UV divergence from the mode-sum similar to the I_3 term in appendix A will still arise in calculating the two-point correlators of the detector, and will never decay out due to the echoes. To get rid of such a UV divergence, again we need to introduce a UV cutoff $n_{\max}$ to exclude the modes with $|n| > n_{\max}$ for k_n or k_n' in our effective theory. Again, to be consistent with the retarded Green's function (2.17) we applied, the UV cutoff here cannot be too small to violate the uncertainty relation.

3.2.2 Linear entropy

In figures 6–9 we show selected numerical results of the two-point correlators and the detector-field entanglement in this model with the initial state (3.13). The degree of entanglement here is characterized by the linear entropy $S_L = 1 - \mathcal{P}$: the higher the value of S_L, the stronger the entanglement between the detector and the field.

In contrast to the simpler dissipative behavior in Minkowski space, where the time-slices are not compact and the spectrum of the field modes is continuous [17, 30], the behaviors of the two-point correlators $\langle \hat{Q}_A^2 \rangle$, $\langle \hat{P}_A^2 \rangle$, $\langle \hat{Q}_A, \hat{P}_A \rangle$, and the linear entropy S_L in $\mathbf{S}^1 \times \mathbf{R}_1$ are more complicated. At early times before the first echo arrives ($t/L < 1$), the correlators and S_L do behave similarly to their Minkowskian counterparts (also see
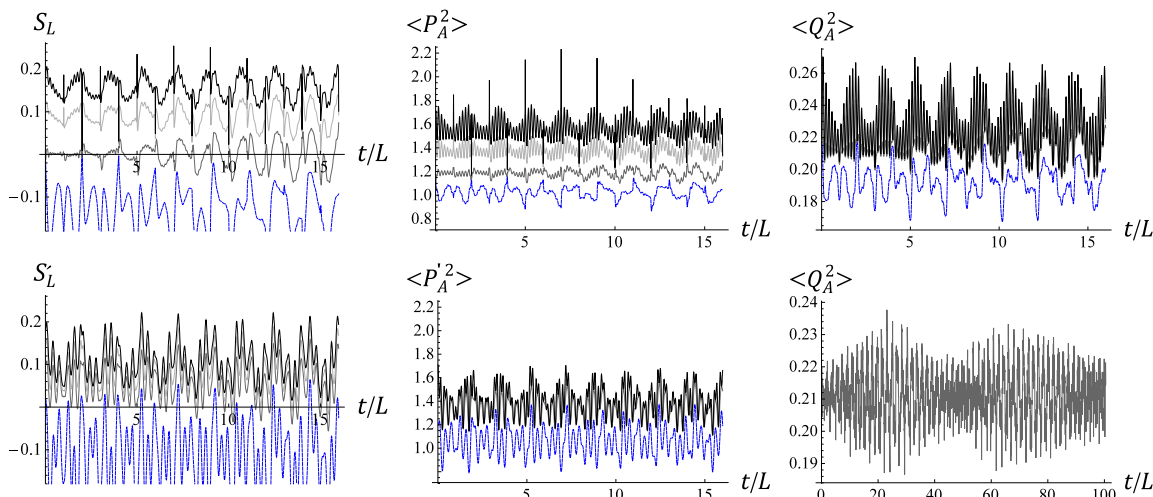
Figure 7. Results similar to those in figure 6 with the same values of the parameters except $\varepsilon = -1$ here for the twisted field. The dark-gray, light-gray, and black curves represent the results contributed by the modes with $k'_n = [n - (1/2)]/R$ from $|n| = 1$ up to $|n| = 10$, 100, and 1000, respectively, while the blue-dashed curve is contributed only by the four modes with $|n| = 3$ and 4, which have the closest frequencies to the detector's. There seems to be no beat with period longer than L in the upper plots. However, the beats with very long period (about $50 \times L$) emerge in the lower-right plot (contributed by the modes with $|n| = 1$ to 10). They are produced by the three dominant eigen-modes at eigen-frequencies $(1.87266, 2.30377, 2.75063)$ [around $(\omega_3, \Omega_0, \omega_4)$]. Indeed, the beat frequency is about $||2.30377 - 1.87266| - |2.75063 - 2.30377|| \approx 0.01575 \approx 2\pi/(48.84L)$ here. The lower-left and lower-middle plots show the results in terms of the unphysical P'_A defined in (2.8). The differences from the results with the kinetic momentum are not as significant as those in the untwisted field: only the spikes around $t = nL$ in the upper plots are smeared.

appendix A). At a large time scale, however, the a-parts of the correlators never decay out, and the beat of the mode function q^A_A in figure 2 is obvious in figure 6, while there is no significant beat in the upper plots of figure 8, as indicated in figure 3. This is also true for the twisted field in figures 7 and 9, though the beats of their mode functions are not shown in this paper.

The behavior of S_L cannot be approximated by including the contributions only by the one or two field modes nearest to resonance with the detector in the v-part of the correlators. Indeed, the beats in the green and blue-dashed curves in the upper plots of figures 6 to 9 are almost gone, since the contributions of $|q^A_A|^2$ (the upper-left plot in figure 2) and $|q^{k_3}_A|^2$ (the second plot from the left in the upper row of figure 4) have the same order of magnitude but are out of phase. Moreover, as we mentioned above, similar few-mode approximations can violate the uncertainty relation in some periods of time in the system's history due to the inconsistency with the retarded Green function. During these periods, the value of S_L becomes negative and so unphysical. To get rid of this one has to include enough field modes in the v-part of the correlators (at least $n_{max} \sim 100$ in figures 6–9).
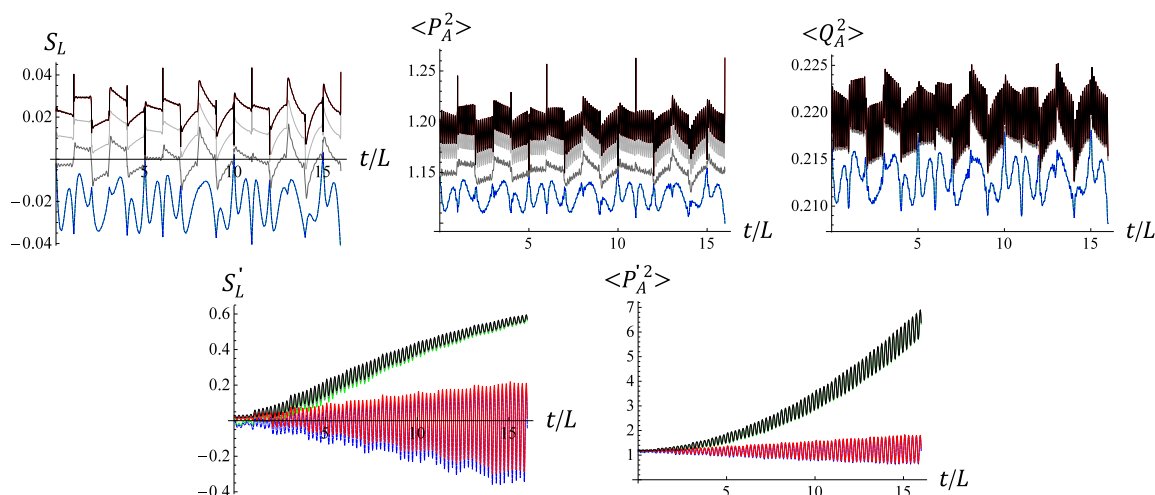
Figure 8. Another example in the normal (untwisted) field, for comparison with figures 3 and 5. The upper plots are the results with the physical P_A, and the lower plots are those with the unphysical P'_A. The dark-gray, light-gray, and black solid curves represent the results contributed by the modes ω_{k_n} from $|n| = 0$ up to $|n| = 10$, 100, and 1000, respectively, while the blue-dashed curve is contributed only by the zero mode and the modes with $|n| = 4$ and 5, which are the modes with the frequencies closest to the detector's. The blue-dashed ($|n| = 4, 5$) and red-dotted curves ($|n| = 1$ to 1000) are obtained from the green and the black curves with the contributions by the zero mode removed, respectively. As in figure 3, no significant beat can be observed here.
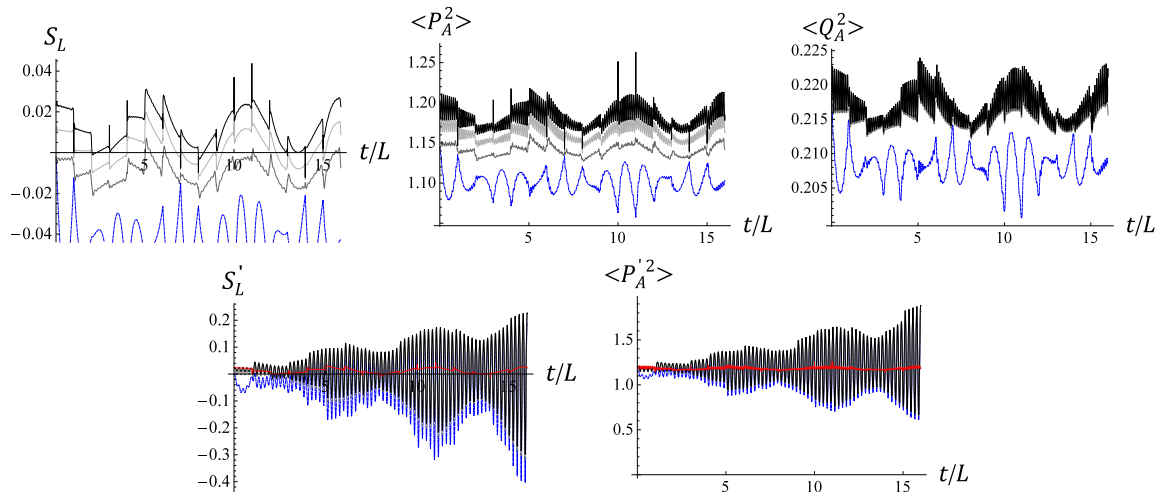

Figure 9. The same parameters as those in figure 8 except here the detector is in the twisted field ($\varepsilon = -1$). (Upper row) The dark-gray, light-gray, and black solid curves represent the results contributed by the modes $\omega_{k'_n} = |n - (1/2)|/R$ from $n = 1$ up to $n = 10$, 100, and 1000 respectively, while the blue-dashed curve is contributed only by the modes with $n = 5$, whose mode frequency is the closest to the detector's. In contrast to the case with the untwisted field in figure 8, here the beating behavior is obvious. (Lower row) $\langle \hat{P}'^2_A \rangle$ and S'_L contributed by the unphysical momentum P'_A. The red curves represent $\langle \hat{P}^2_A \rangle$ and S_L (the black curves in the upper row) for comparison.

The higher-frequency modes are responsible for the small oscillations on top of the beat at the frequency about 2Ω in the weak coupling limit. As the UV cutoff $n_{\max}$ increases, such small oscillations of $\langle \hat{Q}_A^2 \rangle$ and $\langle \hat{P}_A^2 \rangle$ will be amplified, while the whole evolution curves of $\langle \hat{Q}_A^2 \rangle$, $\langle \hat{P}_A^2 \rangle$, and thus S_L, will be elevated as well. Including the higher-frequency modes further helps to resolve the spikes of the evolution curve of $\langle P_A^2 \rangle$ occurring around $t = nL$, $n = 1, 2, 3, \ldots$ as shown in the middle plots in the upper rows of figures 6–9. These spikes are due to constructive interferences occurring periodically at $t = nL$ when $e^{i\omega_{n'} t} = 1$ for all $\omega_{n'} = |k_{n'}|$ or $|k'_{n'}|$, $n' = 1, 2, 3, \ldots$ such that the mode sum of $\langle P_A^2 \rangle$ get an additional logarithmic divergence. More explicitly, the terms in $\langle \hat{P}_A^2(t) \rangle_{\mathrm{v}}$ corresponding to $C_3(t)$ in (A.5) goes to the counterpart of I_3 in $\mathbf{S}^1 \times \mathbf{R}_1$ as $t \to nL$ (in $\mathbf{R}_1^1$ this only occurs as $t \to 0$). While the value of $\langle \hat{P}_A^2 \rangle$ varies significantly at these moments, once the UV cutoff is introduced, the amplitudes of the spikes relative to their neighborhoods will be finite. They can be higher or lower than their neighborhood (see the factor of the C_3-term in (A.5)), but will never overwhelm those which have been corresponding to the I_3 terms for $t \neq nL$ to make the corrections to $\langle P_A^2 \rangle$ from higher-frequency modes negative.

In the lower-right plot of figure 7, while the frequency of the detector is near resonant to none of the field mode, the curves happen to show a beat with a very long period. Such a beat is produced mainly by three eigen-frequencies rather than two. When the free detector frequency is almost, but not exactly, located at the middle point between two frequencies of the free field modes, and L has a proper value, the three eigen-modes with eigen-frequencies around these three natural frequencies will dominate. While the difference between every two dominant eigen-frequencies is $O(1/R)$, which gives no beat beyond the period L of the echoes, the small difference between 1) the frequency difference of the middle and the lower modes, and 2) the difference of the higher and the middle modes, stands out and sets a beat frequency. Note that if the spacing $1/R$ in the frequency spectrum of the free field is too large, only the eigen-mode with frequency around the free detector's will dominate and so no significant beats will be observed; if $1/R$ is too small, there will be so many dominant eigen-modes that the evolution becomes complicated.

3.2.3 Effects of the zero-mode

For the untwisted field, the curves with or without the zero-mode contribution (e.g. the black and red-dotted curves, respectively, in figures 6 and 8) are almost indistinguishable in the results with the kinetic momentum $\hat{P}_A$. The zero-mode contributions to the v-parts of the two-point correlators with P_A are not important here since we have chosen the initial state of the zero-mode having the minimal uncertainty. Just like other field modes, a slight change of the initial state of the zero-mode will change the results of the correlators and S_L slightly.

When S_I and P_A are replaced by the gauge-dependent S'_I and P'_A, the zero-mode will make $\langle \hat{P}'^2_A \rangle$ growing as t^2 indefinitely and so S_L also growing in time at large time scales (see the lower plots of figures 6 and 8). This behavior, taken on face value, may be construed as the detector-field entanglement increases forever. However, since P'_A is a gauge-dependent quantity, this ill-behavior is not physically meaningful. Only the entanglement in terms of the physical P_A matters.
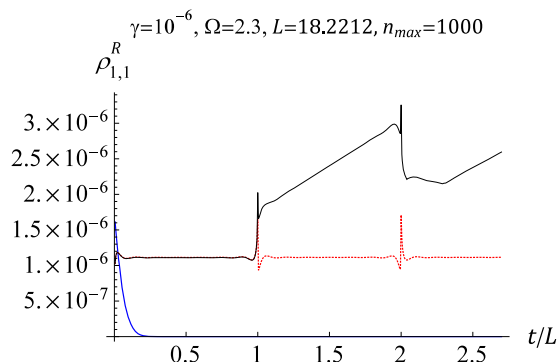
Figure 10. Our nonperturbative result for the probability of finding the detector in the first excited state (black), is compared with (3.17) obtained by first-order TDPT with finite duration of interaction (red dotted) in the perturbative regime ($\gamma \ll \Omega$). One can see that the deviation becomes significant as early as $t \approx L$. For comparison, we also show the first-order TDPT result (3.18) with infinite duration of interaction weighted by a Gaussian switching function with width t (blue). Note that $L\gamma \ll 1$ even for $t > L$ in this plot.

3.3 Comparison with perturbative results

3.3.1 On the zero mode

The transition probability of a single UD' detector in the untwisted field from the initial ground state to the first excited state of the detector, obtained using the time-dependent perturbation theory (TDPT), depend on the initial two-point correlator of the conjugate momentum of the zero mode, $\langle \hat{\Pi}_{k_0}^2(0) \rangle \equiv {}_z\langle 0_L | \hat{\Pi}_{k_0}^2(0) | 0_L \rangle_z$, but is independent of the initial correlator of the zero mode itself, $\langle \hat{\Phi}_{k_0}^2(0) \rangle \equiv {}_z\langle 0_L | \hat{\Phi}_{k_0}^2(0) | 0_L \rangle_z$ [27]. Accordingly the authors of [27] claimed that the effect of the zero mode in the UD' detector theory defined in $\mathbf{S}^1 \times \mathbf{R}_1$ can be suppressed by choosing a suitable initial state such that $\langle \hat{\Pi}_{k_0}^2(0) \rangle$ is very small. They pointed out that this is not possible for the usual UD detector with $Q\Phi$ coupling in $\mathbf{S}^1 \times \mathbf{R}_1$ since in that case $\langle \hat{\Phi}_{k_0}^2(0) \rangle$ also enters the response function and will become large if $\langle \hat{\Pi}_{k_0}^2(0) \rangle$ is squeezed (due to the uncertainty relation $\langle \hat{\Phi}_{k_0}^2(0) \rangle \langle \hat{\Pi}_{k_0}^2(0) \rangle \geq (\hbar/2)^2$).

From eqs. (20)–(23) in [30], we have seen that after taking the weak coupling limit $\gamma \ll \Omega$ for the complete expression of the transition probability, the leading term will be proportional to the $O(\gamma)$ part of $\langle \hat{P}_A^2 \rangle + \Omega_0^2 \langle \hat{Q}_A^2 \rangle$ ($m_0 = 1$ here). If we choose the static initial state so that ${}_z\langle 0_L | \{ \hat{\Phi}_{k_0}(0), \hat{\Pi}_{k_0}(0) \} | 0_L \rangle_z = 0$, the zero mode contributions to $\langle \hat{Q}_A^2 \rangle$ and $\langle \hat{P}_A^2 \rangle$ will be $(\text{Re}\, q_A^{k_0})^2 \langle \hat{\Phi}_{k_0}^2(0) \rangle + (\text{Im}\, q_A^{k_0})^2 \langle \hat{\Pi}_{k_0}^2(0) \rangle$ and $(\text{Re}\, p_A^{k_0})^2 \langle \hat{\Phi}_{k_0}^2(0) \rangle + (\text{Im}\, p_A^{k_0})^2 \langle \hat{\Pi}_{k_0}^2(0) \rangle$, respectively. When $0 < t < L$, from (3.5) one sees that both $q_A^{k_0}$ and $p_A^{k_0} = \partial_t q_A^{k_0}$ are purely imaginary, which implies that $\text{Re}\, q_A^{k_0} = \text{Re}\, p_A^{k_0} = 0$ for all time according to eq. (3.2). Thus indeed, the initial variance $\langle \hat{\Phi}_{k_0}^2(0) \rangle$ of the zero mode are totally irrelevant to the two-point correlators of detector A in the untwisted field. The zero-mode contribution to the dynamics of the combined system in our model depends on $\langle \hat{\Pi}_{k_0}^2(0) \rangle$ only.

3.3.2 On the validity of perturbative transition probability

In figure 10, we show the transition probability from the ground state $|g\rangle$ to the first excited state $|e_1\rangle$ of a UD' detector initially in the vacuum state of an untwisted field obtained

by our nonperturbative method (black), and the first-order TDPT result (red dotted) [30] given by

$$\rho_{1,1}^R \approx \lambda^2 \big|\langle e_1|\hat{Q}_A(0)|g\rangle\big|^2 \int_0^t dt_1 \int_0^t dt_2 e^{-i\Omega_0(t_1-t_2)} \partial_{t_1}\partial_{t_2}\langle 0|\hat{\Phi}_{x=0}^{[0]}(t_1)\hat{\Phi}_{x=0}^{[0]}(t_2)|0\rangle$$

$$= \frac{2\gamma}{\Omega_0 L^2}\left\{\frac{1-\cos\Omega_0 t}{\Omega_0^2} + 4\pi\sum_{n=1}^{n_{\max}} n\left[\frac{1-\cos\left(\frac{2\pi n}{L}+\Omega_0\right)t}{\left(\frac{2\pi n}{L}+\Omega_0\right)^2}\right]\right\}, \tag{3.17}$$

where $\hbar = 1,$[5] $\hat{\Phi}_x^{[0]}(t) = \sum_k (2\tilde{\omega}_k)^{-1/2}\big[\phi_x^{[0]k}(t)\hat{b}_k + \phi_x^{[0]k*}(t)\hat{b}_k^\dagger\big]$ is the free field operator, and $\big|\langle e_1|\hat{Q}_A(0)|g\rangle\big|^2 = 1/(2\Omega_0)$. One can see that the TDPT result (3.17) deviates significantly (still $O(\gamma)$) from the nonperturbative result as early as $t \approx L$ when the first echo returns, though the echoes appear to be higher-order effects in the equation of motion (3.1). For further comparison, we also present the perturbative result (the blue curve in figure 10)

$$\rho_{1,1}^R \approx \frac{\lambda^2}{2\Omega_0}\int_{-\infty}^{\infty}dt_1\int_{-\infty}^{\infty}dt_2\chi_t(t_1)\chi_t(t_2)e^{-i\Omega_0(t_1-t_2)}\partial_{t_1}\partial_{t_2}\langle 0|\hat{\Phi}_{x=0}^{[0]}(t_1)\hat{\Phi}_{x=0}^{[0]}(t_2)|0\rangle$$

$$= \frac{\gamma t^2}{\Omega_0 L^2}\left\{e^{-t^2\Omega_0^2/(8\pi)} + 4\pi\sum_{n=1}^{n_{\max}} n\exp\left[-\frac{t^2}{8\pi}\left(\frac{2\pi n}{L}+\Omega_0\right)^2\right]\right\}, \tag{3.18}$$

with the Gaussian switching function $\chi_t(\tau) \equiv 2e^{-\pi(2\tau/t)^2}$ so that the width $t = \int_{-\infty}^{\infty}\chi_t(\tau)$ $d\tau = \int_0^t d\tau$ corresponds to the duration of interaction in eq. (3.17). We find that the Gaussian switching function greatly suppresses the perturbative transition probability (3.18), which decays very quickly as the effective interaction time t increases. Comparing (3.18) with (3.17), one can see that at a fixed t, the summand of the summation $\sum_{n=1}^{n_{\max}}$ goes like ne^{-n^2} for large n in (3.18), and n^{-1} in (3.17). So (3.18) receives much less contributions from the short-wavelength modes than (3.17) does if $n_{\max}$ is large enough.

4 Two-detector case

Consider two identical detectors A and B at rest with natural frequencies $\omega_A = \omega_B = \Omega_0$, located at $x = z_A^1 = 0$ and $x = z_B^1 = R\pi = L/2$, respectively, as shown in figure 1 (left) and (middle). Substituting the expansions (2.13) and (2.14) into the Heisenberg equations of motion for the operators yields

$$(\partial_t^2 + 2\gamma\partial_t + \Omega_0^2)q_{A(B)}^\mu(t) =$$
$$- \lambda\partial_t\phi_{z_A^1(z_B^1)}^{[0]\mu}(t)$$
$$- \frac{\lambda^2}{2}\sum_{n'=1}^{\infty}\Big\{(\varepsilon^{n'}+\varepsilon^{n'})\theta(t-n'L)\partial_t q_{A(B)}^\mu(t-n'L)$$
$$+ (\varepsilon^{n'}+\varepsilon^{n'+1})\theta\big(t-[n'-(1/2)]L\big)\partial_t q_{B(A)}^\mu\big(t-[n'-(1/2)]L\big)\Big\}, \tag{4.1}$$

where $\mu = A, B, k_n$ (untwisted) or k_n' (twisted field), $n \in \mathbf{Z}$, $\phi_x^{[0]A} = \phi_x^{[0]B} \equiv 0$, $\phi_x^{[0]k}(t) \equiv e^{-i(|k|t-kx)}$ for $k \neq 0$ (k can be k_n or k_n'), and $\phi_x^{[0]k_0}(t) \equiv 1 - (i/L)t$ for the zero-mode.

---

[5]Note that it should be $\hbar^{-3}$ instead of $\hbar^{-1}$ in the overall factor of the r.h.s. of eq. (26) in [30].

From the setups in the extended coordinates (figure 1 (middle) and (right)), one can see that the *classical* dynamics for an individual detector and the untwisted field in the cases with two or more identical detectors would be equivalent to the dynamics of the detector and the untwisted field in the single detector case: in the two-detector case $Q_A(t)$ is affected by $Q_B(t - (L/2))$ with identical solutions to $Q_A(t - (L/2))$ in the one-detector case. However, this is not true for the mode-functions in quantum theory. In (4.1), $q_A^A(t)$ is affected by $q_B^A(t)$ rather than $q_B^B(t)$, and the initial condition for the former is $q_B^A(t < (L/2)) = 0$, which is different from (3.3) for $q_B^B(t < (L/2)) = q_A^A(t < (L/2))$.

Suppose the initial state of the combined system at $t = 0$ is a factorized state,

$$|\psi(0)\rangle = |q_A, q_B\rangle \otimes |0_L\rangle, \tag{4.2}$$

which is a direct product of a two-mode squeezed state of the detectors $|q_A, q_B\rangle$, or in the Wigner function representation,

$$\rho_{AB}(0) = \frac{1}{\pi^2} \exp -\frac{1}{2} \big[\beta^2 (Q_A + Q_B)^2 + \beta^{-2}(P_A + P_B)^2$$
$$+ \alpha^{-2}(Q_A - Q_B)^2 + \alpha^2 (P_A - P_B)^2 \big] \tag{4.3}$$

with constant parameters α and β [17], and the vacuum state of the field $|0_L\rangle$. Again, for the untwisted field, we further factorize the field state into $|0_L\rangle = |0_L\rangle_{\mathrm{nz}} \otimes |0\rangle_{\mathrm{z}}$ where $|0\rangle_{\mathrm{z}}$ is the initial state of the zero mode giving $_{\mathrm{z}}\langle 0_L|\hat{\phi}_{k_0}^2(0)|0_L\rangle_{\mathrm{z}} = {}_{\mathrm{z}}\langle 0_L|\hat{\pi}_{k_0}^2(0)|0_L\rangle_{\mathrm{z}} = \hbar/2$.

4.1 Untwisted field

In the untwisted field, writing $q_\pm^\mu = (q_A^\mu \pm q_B^\mu)/\sqrt{2}$, the equations of motion (4.1) for the mode functions can be simplified to

$$(\partial_t^2 + 2\gamma\partial_t + \Omega_0^2)q_\pm^\mu(t)$$
$$= -\frac{\lambda}{\sqrt{2}}\partial_t \Big[\phi_0^{[0]\mu}(t) \pm \phi_{L/2}^{[0]\mu}(t) \Big] - \lambda^2 \sum_{n'=1}^\infty (\pm 1)^{n'} \theta\left(t - n'\frac{L}{2}\right)\partial_t q_\pm^\mu\left(t - n'\frac{L}{2}\right) \tag{4.4}$$
$$= -\frac{\lambda}{\sqrt{2}}\mathcal{F}_\pm^\mu(t) \pm \theta\left(t - \frac{L}{2}\right)(\partial_t^2 - 2\gamma\partial_t + \Omega_0^2)q_\pm^\mu\left(t - \frac{L}{2}\right), \tag{4.5}$$

where

$$\mathcal{F}_\pm^\mu(t) = \partial_t\Big[\phi_0^{[0]\mu}(t) \pm \phi_{L/2}^{[0]\mu}(t) \Big] - \theta\left(t - \frac{L}{2}\right)\partial_t\left[\pm \phi_0^{[0]\mu}\left(t - \frac{L}{2}\right) + \phi_{L/2}^{[0]\mu}\left(t - \frac{L}{2}\right) \right]. \tag{4.6}$$

When $0 < t \leq L/2$, $\mathcal{F}_\pm^{k_n}(t) = i|k_n|e^{-i|k_n|t}[1 \pm (-1)^n]$ for $k_n \neq 0$, $\mathcal{F}_+^{k_0}(t) = -2i/L$, and $\mathcal{F}_\pm^A = \mathcal{F}_\pm^B = \mathcal{F}_-^{k_0} = 0$. When $t > L/2$, all the components of $\mathcal{F}_\pm^\mu$ vanish. Compared with (3.2), one can see that the equations for q_+ and q_- in (4.5) are almost equivalent to the ones for a single detector in the untwisted and twisted fields, respectively, in S^1 with circumference $L/2$, except that the force terms $\mathcal{F}_\pm^{k_n}(t)$ and $\mathcal{F}_\pm^{k_0}(t)$ driven by vacuum fluctuations of the field in (4.5) are different from their counterpart in (3.2).

The above delayed differential equations will be solved together with the conditions that for $0 \leq t < L/2$, $q_A^B(t) = q_B^A(t) = 0$, $q_A^A(t) = q_B^B(t)$ are given by eq. (3.3), and $q_A^k(t) = q_B^k(t)$ are given by (3.4) and (3.5), before the mutual influences set in.

4.1.1 Eigen-frequencies

Substituting the ansatz $q_\pm^{\mathbf{d}} \approx \int d\omega_\pm \tilde{q}_\pm^{\mathbf{d}}(\omega_\pm) e^{i\omega_\pm t}$, $\mathbf{d} = A, B$ into (4.5), we find

$$-\omega_+^2 + \Omega_0^2 = -2\gamma\omega_+ \cot(\omega_+ L/4)\,, \tag{4.7}$$

$$-\omega_-^2 + \Omega_0^2 = 2\gamma\omega_- \tan(\omega_- L/4)\,, \tag{4.8}$$

which are almost the same as (3.7) and (3.11) in the one-detector case except L there has been replaced by $L/2$ here. The solutions of the above two equations are the eigen-frequencies of the mode functions $q_\pm^{\mathbf{d}}$.

In weak coupling limit $\gamma \ll \Omega_0$, if Ω_0 is not very close to $2n\pi/L = n/R$, $n \in \mathbf{N}$, the two detectors with the same natural frequency Ω_0 will be mixed together by the effective coupling mediated by the field, and so the dominant eigen-modes will split into $\omega_+ \approx \Omega_0 + \gamma \cot(\Omega_0 L/4)$ from (4.7) and $\omega_- \approx \Omega_0 - \gamma \tan(\Omega_0 L/4)$ from (4.8). These two eigen-frequencies can be quite close to each other, and so the beat frequency of $q_{A(B)}^{\mathbf{d}} = (q_+^{\mathbf{d}} \pm q_-^{\mathbf{d}})/\sqrt{2}$ will be approximately

$$\Delta \approx \gamma \left| \cot\frac{\Omega_0 L}{4} + \tan\frac{\Omega_0 L}{4} \right| = \frac{2\gamma}{|\sin(\Omega_0 L/2)|}\,. \tag{4.9}$$

When $\Omega_0 \approx (2n+1)\pi/L$, the above beat frequency will reach the lowest value $\Delta \approx 2\gamma$ in the weak coupling limit.

When the natural frequency of the detectors is very close to the frequency of a free field mode, namely, $\Omega_0 \approx 2n\pi/L$, with some positive integer n large enough, the two detectors and the field mode will split into three eigen-modes at frequencies $2n\pi/L$ and $(2n\pi/L \pm \Delta)$, where $\Delta \approx \sqrt{\gamma/\pi}$ will be the beat frequency in this case. This is a half of the beat frequency 2Δ we obtained below (3.8) in the one-detector case. If the eigen-frequency around $2n\pi/L$ is not exactly at the averaged value of the two eigen-frequencies around $(2n\pi/L \pm \Delta)$, when L has a proper value, there will be beats with an even longer time scale similar to the one in figure 7. In other parameter range of L, the beating behavior may disappear or get more complicated.

4.1.2 Super-radiant mode and instability?

In Minkowski space, the modes for two detectors similar to q_+ here (eq. (20) in [17]) can be interpreted as the super-radiant modes since the dissipation rate is about twice of the one for the single detector there. However here in a similar limit, $L \ll \gamma \ll \Omega_0$, expanding $q_+\big(t - (L/2)\big) = q_+(t) - (L/2)\partial_t q_+(t) + \ldots$, eq. (4.4) gives

$$\frac{L}{2}\left[\left(1 + \frac{\gamma L}{2} + \frac{L^2\Omega_0^2}{24}\right)\partial_t^3 q_+ - \left(2\gamma + \frac{1}{4}\Omega_0^2 L\right)\partial_t^2 q_+ + \left(\frac{8\gamma}{L} + \Omega_0^2\right)\partial_t q_+ \right] \approx 0\,, \tag{4.10}$$

by assuming q_+ varies slowly in time. This implies $\partial_t q_+ \sim e^{(-\Gamma \pm i\omega)t}$ with $\Gamma^2 \equiv (\gamma + \Omega_0 L^2/8)^2 \ll \omega^2 \equiv \Omega_0^2 + (8\gamma/L)$. ω is nothing but the lowest eigen-frequency obtained from (4.7) in the same limit (where $\cot(L\omega/4) \approx 4/(L\omega)$). So q_+ here oscillates in the lowest eigen-frequency rather than decays in a quicker rate. The behaviors of such solutions are quite different from the super-radiant modes in [17] since the space here is extremely

compact: the size of the space L is the same order of the separation of the detector $L/2$, both are extremely small.

For two UD detectors at rest in (3+1) dimensional Minkowski space, when the separation is small enough, the detectors will become unstable [17]. Now in an Einstein cylinder, when the value of L is small, would we get runaway solutions for the mode functions of the detector(s)?

The instability in the analysis in [17] is due to the fact that the amplitude of the retarded fields in (3+1)D Minkowski space diverges as one approaches to the point-source. However, in our (1+1)D Einstein cylinder the retarded solution of a massless scalar field is regular around the source. Thus a small value of L in our model will produce no instability. Indeed, in our calculation we always obtain real eigen-frequencies. Imaginary eigen-frequencies never show up when we take L to 0+.

4.1.3 Entanglement dynamics

Some examples of the entanglement dynamics for identical detectors A and B located at $x = 0$ and $L/2$, respectively, in the untwisted field are illustrated in figure 11. The degree of entanglement between the two detectors is characterized by the logarithmic negativity [31, 32] $E_\mathcal{N} = \max\{0, -\log_2 2c_-\}$ evaluated around the future light cone (EnLC) of detector A, which is essential in quantum teleportation from detector A to detector B [3]: the value of the $E_\mathcal{N}$ of the EnLC is a monotonic function of the upper bound of the optimal fidelity of coherent-state teleportation [33]. Here c_- is the lowest symplectic eigenvalue of the partially transposed covariance matrix in the reduced state of the detector pair. The higher UV cutoff $n_{\max}$ is introduced, or the larger initial variance $\langle \hat{\Pi}_{k_0}^2 \rangle$ of the zero mode is given, the lower EnLC will be.

In figure 11 (upper-left), one can see that $|q_A^A|^2$ behaves like $(1 + \cos t\Delta)/2$, and $|q_A^B|^2$ like $(1 - \cos t\Delta)/2$ with the beat frequency Δ given in (4.9). Both $|q_A^A|^2$ and $|q_A^A|^2$ have the beat period $2\pi/\Delta$, which is two times longer than the results in the one-detector case in figure 2. In the other plots of figure 11 with different choices of the parameters α and β for the initial two-mode squeezed state of the detector pair, the $E_\mathcal{N}$ of the EnLC of detector A (black curves) in each case shows the same beating behavior of the mode function squared $|q_\mathbf{d}^{\mathbf{d}'}|^2$, so do the linear entropy S_L of detector A. One can see entanglement creation, sudden-death and revival of the detector pair in the lower plots from the interplay with the field.

The $E_\mathcal{N}$ evaluated on the hypersurfaces of simultaneity (constant t-slices) (EnS) of detector A (gray dashed curves) has a similar beating behavior, but their extrema lag behind the EnLC's in the clock of detector A, so does the linear entropy S_L of detector A, which is a measure of entanglement between a single detector and the rest of the combined system (including the field in addition to the other detector). In the right plots, it appears that S_L of detector A increases as the $E_\mathcal{N}$ of the ENLC does. However, such a tendency is not clear in the lower-left plot, where detectors A and B are initially in a separable product state of their ground states.

In the right plots we further introduce the linear entropy of the detector pair, $S_L^{(2)} = 1 - \mathrm{Tr}(\rho_{AB}^{\mathrm{R}})^2 = 1 - \hbar^2/(4\sqrt{\det V})$, where ρ_{AB}^{R} is the reduced state of the detector pair
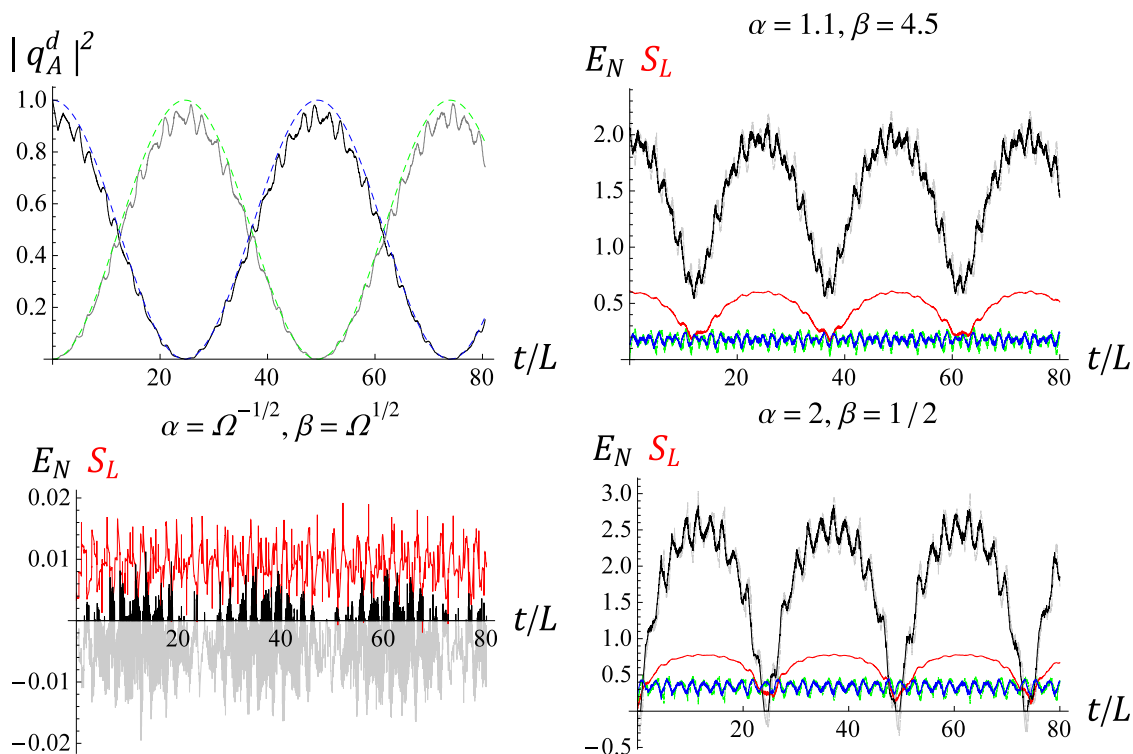
Figure 11. Entanglement dynamics of two UD' detectors contributed by the field-modes with k_n, $|n| = 0, \ldots, 250$, in terms of detector A's clock. Here $\gamma = 0.005$, $\Omega = 2.3$, $L = 4\pi$, and α and β are shown in the plot labels. (Upper left) $|q_A^A|^2$ (black) has a beating behavior like $(1 + \cos t\Delta)/2$ (green-dashed) and $|q_A^B|^2$ (gray) like $(1 - \cos t\Delta)/2$ (blue-dashed) with $\Delta \approx 0.01014 \approx 2\gamma / \sin(\Omega_0 L/2)$ given in (4.9). (Upper-right and lower row) The logarithmic negativity $E_{\mathcal{N}} = \max\{0, -\log_2 2c_-\}$ (black) of the EnLC compared with the $E_{\mathcal{N}}$ of the EnS (gray dashed), the linear entropy S_L of detector A (red), and the linear entropies $S_L^{(2)}$ of the detector pair evaluated around the future light cones (blue) and the hypersurfaces of simultaneity (green dashed) of detector A. The gray part of the curve for the $E_{\mathcal{N}}$ of the EnLC represents $-\log_2 2c_-$ at negative values, where $E_{\mathcal{N}} = 0$. In the lower left plot, both of the two detectors are initially in their ground states. One can see that E_N has a beat frequency 2Δ, so does the linear entropy S_L of detector A in the right plots.

A and B, and V is the covariance matrix of the detector pair. This is a measure of the entanglement between the detector pair and the field, combined as a bipartite system. Similar to $E_{\mathcal{N}}$, the value of $S_L^{(2)}$ can be taken either on the future light cones (blue) or on the hypersurfaces of simultaneity (green dashed curves) of detector A. The extrema of the latter also lag behind the ones of the former. We find that either way $S_L^{(2)}$ does not follow the largest beats of $E_{\mathcal{N}}$. This indicates that the increased entanglement between detectors A and B are mainly influenced by the nonlocal correlations in the field, rather than the correlations between the detectors and the field.

4.2 Twisted field

In the twisted field, q_A^μ and q_B^μ will not influence each other if detectors A and B are located exactly at $x = 0$ and $x = L/2$ in $\mathbf{S}^1$. This is because in detector A's point of

view, the retarded field from detector B or it's image at $x = \left(n' - (1/2)\right)L$, $n' = 1, 2, 3, \ldots$, in the extended coordinates carries a $\varepsilon^{n'}$ factor, but the field from $x = \left(-n' + (1/2)\right)L$ carries an $\varepsilon^{n'+1}$ factor and cancel the former when $\varepsilon = -1$ (note that $L/2$ is in the domain $(-L/2, L/2]$ for x in the restricted coordinates, but $-L/2$ is not). So the situation of our setup for the twisted field looks rather simple: $q_A^B = q_B^A = 0$ for all time, and the equations of motion (4.1) reduce to eqs. (3.1) and (3.2) for single detectors with the subscript $\mathbf{d} = A$ generalized to $\mathbf{d} = A, B$ while $\phi_0^{[0]k_n}(t)$ for $\mathbf{d} = A$ in eq. (3.1) or (3.2) is replaced by $\phi_{L/2}^{[0]k_n}(t)$ when $\mathbf{d} = B$. Their eigen-frequencies are thus identical to those in section 3.1.2 with the same parameter values.

4.2.1 Vanishing v-parts of the cross correlators

The quantum correlation initially in the twisted field will never be converted to the detector-detector entanglement since the v-parts of the cross correlators always vanish here. Indeed, writing $\omega_n' = (n - 1/2)/R$, $n = 1, 2, 3, \ldots$, so that $k_n' = \omega_n'$ for $k_n' > 0$, and $k_{n'}' = -\omega_{n'+1}'$ when $k_{n'}' < 0$, $n' = 0, 1, 2, \ldots$. From eq. (3.2), one has $q_A^{\omega_n'}(t) = q_A^{-\omega_n'}(t)$ and $p_A^{\omega_n'}(t) = p_A^{-\omega_n'}(t)$ since $\partial_t \phi_0^{[0]\omega_n'}(t) = -i\omega_n' e^{-i\omega_n' t} = \partial_t \phi_0^{[0]-\omega_n'}(t)$. Similarly, since $\partial_t \phi_{L/2}^{[0]\omega_n'}(t) = e^{i\omega_n'(L/2)}\partial_t \phi_0^{[0]\omega_n'}(t) = -i(-1)^n \partial_t \phi_0^{[0]\omega_n'}(t) = -\partial_t \phi_{L/2}^{[0]-\omega_n'}(t)$, one can see that $q_B^{\omega_n'}(t) = iq_A^{\omega_n'}(t) = -q_B^{-\omega_n'}(t)$ and $p_B^{\omega_n'}(t) = ip_A^{\omega_n'}(t) = -p_B^{-\omega_n'}(t)$. These imply

$$
\begin{aligned}
\langle \hat{\mathcal{R}}_A(t)\hat{\mathcal{R}}'_B(t')\rangle_{\mathrm{v}} &= \sum_{n \in \mathbf{Z}} \frac{\hbar}{2|k_n'|} \mathrm{Re}\left\{\left[\varrho_A^{k_n'}(t)\right]^* \varrho_B'^{k_n'}(t')\right\} \\
&= \sum_{n>0} \frac{\hbar}{2\omega_n'} \mathrm{Re}\left\{\left[\varrho_A^{\omega_n'}(t)\right]^* \varrho_B'^{\omega_n'}(t') + \left[\varrho_A^{-\omega_n'}(t)\right]^* \varrho_B'^{-\omega_n'}(t')\right\} \\
&= \sum_{n>0} \frac{\hbar}{2\omega_n'} \mathrm{Re}\left\{\left[\varrho_A^{\omega_n'}(t)\right]^* \left(\varrho_B'^{\omega_n'}(t') + \varrho_B'^{-\omega_n'}(t')\right)\right\} = 0\,,
\end{aligned}
\tag{4.11}
$$

where $(\mathcal{R}, \varrho), (\mathcal{R}', \varrho') = (Q, q)$ or (P, p).

4.2.2 Entanglement dynamics

Some examples for the dynamics of the EnLC between the two detectors in our setup in the twisted field are shown in figure 12 with the same values of the parameters as those in figure 11 except $\varepsilon = -1$. One can see that the entanglement dynamics in this setup have the same beating behavior as $|q_A^A|^2$ rather than the combination of $|q_A^A|^2$ and $|q_A^B|^2$ for the untwisted field. The beat frequency is the frequency difference between the dominant eigen-modes of $|q_A^A|^2$ $(=|q_B^B|^2)$ around Ω, which can be obtained from (3.11).

The linear entropy S_L of detector A in the upper-right plot of figure 12 shows the same tendency of increase or decrease as $E_{\mathcal{N}}$ of the EnLC, very much like the case with the untwisted field (the upper-right of figure 11). However, in the lower row of figure 12 the tendency is opposite: S_L increases as the value of $E_{\mathcal{N}}$ or $-\log_2 2c_-$ decreases. If we vary the value of α and β continuously, there will be a continuous crossover between the former and the latter behaviors, where the S_L curves have valleys both around the peaks and the valleys of $E_{\mathcal{N}}$.
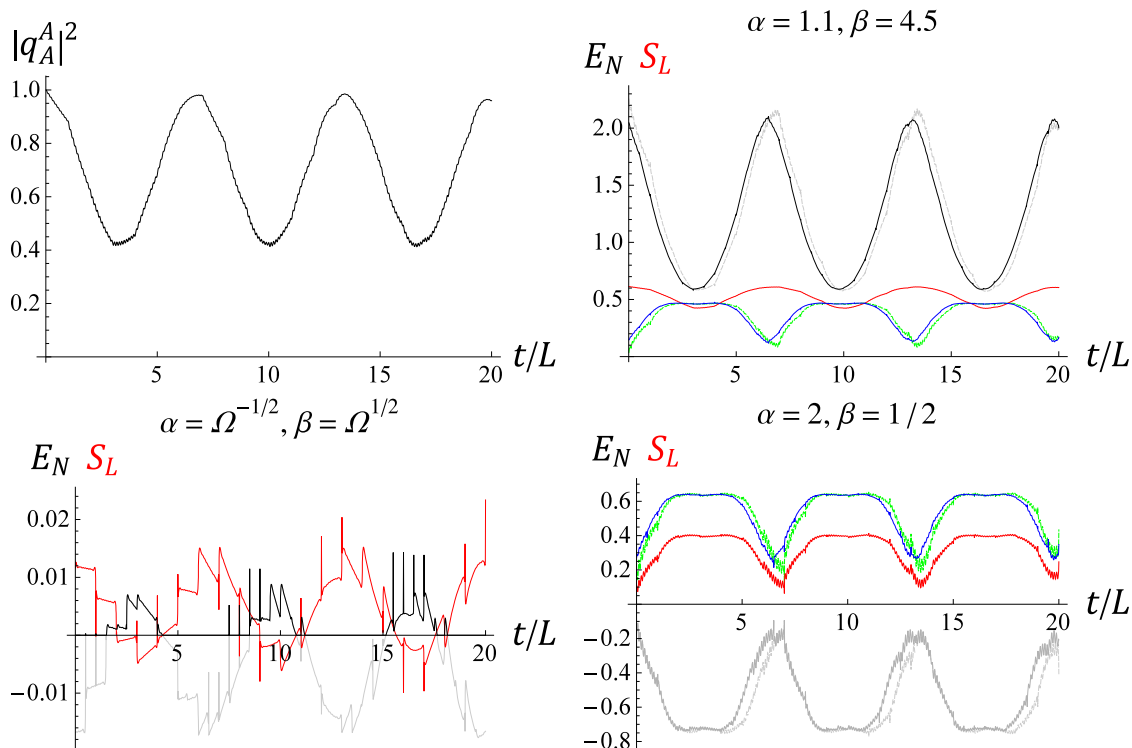
Figure 12. Entanglement dynamics of two UD' detectors in the twisted field, contributed by the field-modes with k'_n, $|n| = 1, \ldots, 1000$. All the parameters have the same values as those in figure 11 except $\varepsilon = -1$. (Upper-Left) The evolution of $|q_A^A|^2$. ($|p_A^A|^2 \approx \Omega^2 |q_A^A|^2$ with this weak coupling.) The beat frequency is about 0.0747, which is the frequency difference of the two dominant eigen-modes obtained from (3.11). (Upper-right and lower row) The curves represent the quantities similar to those in figure 11. One can see that $E_\mathcal{N}$ of the EnLC (black) has the same beating behavior as the mode functions. Note that the entanglement creation in the lower-left plot for the case with the initial state as the ground states of the detectors are not reliable since the linear entropy S_L of detector A (red) is negative whenever the $E_\mathcal{N}$ of the EnLC (black) is positive.

Unlike the case with the untwisted field in figure 11, however, here the EnLC and the $S_L^{(2)}$ around the future light cones of detector A have opposite behaviors, so do their counterparts evaluated on the hypersurfaces of simultaneity. (Again, the extrema of the $E_\mathcal{N}$ of the EnS and the $S_L^{(2)}$ on the hypersurfaces of simultaneity lag behind those evaluated around the future light cones in detector A's clock.) This shows a trade-off between the detector-detector entanglement and the field-detector-pair entanglement, due to the lack of converting the initial nonlocal field-field correlations to the detector-detector correlations in our setup, as we showed earlier in section 4.2.1.

Note that the entanglement creation in the lower-left plot in the case with the initial state as a separable product of the ground states of the detectors are not reliable here since the linear entropy S_L of detector A is negative whenever the $E_\mathcal{N}$ of the EnLC become positive. By extrapolation of $n_{\max}$ from our data, we expect that these EnLC will vanish if we include enough field modes to make S_L of detector A positive at all times (for $n_{\max} \sim O(10^4)$, one may have $S_L > 0$ almost at all times except some moments around $t = nL$ when

the resonance occurs). This would be another difference from the cases with the untwisted field as in the lower-left plot of figure 11, where the detector-detector entanglement can be created by the interplay with the field even if the detector pair was started with the same initial states.

5 Summary and discussion

5.1 Twisted field, untwisted field, and zero mode

The Einstein cylinder, with the topology $\mathbf{S}^1 \times \mathbf{R}_1$, possesses two inequivalent configuration spaces for a real scalar field $\Phi_x(t)$ [9, 10, 12]. The normal (untwisted) field satisfies the periodic boundary condition $\Phi_x(t) = \Phi_{x+L}(t)$ where L is the circumference of $\mathbf{S}^1$, and the twisted field satisfies the anti-periodic boundary condition $\Phi_x(t) = -\Phi_{x+L}(t)$.

The untwisted massless scalar field contains a zero mode (with $\omega_0 = |k_0| = 0$), which is constant in space [27]. It cannot be simply excluded, otherwise the retarded Green's function of the field will violate causality. Due to its singular normalization, however, one has to deal with the zero mode separately from other modes. In terms of the kinetic momenta $P_{\mathbf{d}} = \partial_t Q_{\mathbf{d}}$ associated with the interaction action S_I in (2.3), the effect of the zero mode on the dynamics is similar to those from other modes. If we choose S_I' in (2.7) instead, which yields the canonical momenta $P_{\mathbf{d}}' = \partial_t Q_{\mathbf{d}} + \lambda \Phi_{z_{\mathbf{d}}^1}$, the zero mode turns out to make the two-point correlator of the field amplitudes and the correlators of the canonical momenta of the UD' detectors grow indefinitely, while the energy of the combined detector-field system remains constant, and the energy of each subsystem remains bounded. The ill behavior in the theory with S_I' is simply an illusion when describing the system in terms of the gauge-dependent variables $P_{\mathbf{d}}'$.

The dynamics of the detectors in the twisted field is simpler. There is no zero mode, and the correlators of the detectors never grow indefinitely. Moreover, in the two-detector case, the detector pair in the twisted field will not influence each other if one detector is located at x and the other is located exactly at $(x + L/2 \mod L)$ in $\mathbf{S}^1$. In this setup the detector-detector mode functions $q_{\mathbf{d}}^{\mathbf{d}'}$ are equivalent to those in the one-detector case, and the quantum correlation initially in the field will never be converted to the detector-detector entanglement since the v-parts of the cross correlators of the detectors always vanish here.

5.2 Eigen-frequencies and beats

While the evolution curve of a mode function at early times looks quite similar to the curve at late times at a time scale with only few orders of echoes (see figure 2), as the time scale of observation increases, the eigen-frequencies emerge in the frequency spectrum and the peaks get sharper.

The discrete eigen-frequencies of the detector-detector mode functions $q_{\mathbf{d}}^{\mathbf{d}'}$ are the solutions of eqs. (3.7), (3.11), and eqs. (4.7)–(4.8) in the one-detector and two-detector cases, respectively. In the weak coupling limit, the eigen-frequencies are close to but not exactly the same as the natural frequencies of the free detectors and the free field modes. The

eigen-frequencies of the detector-field mode functions $q_{\mathbf{d}}^{k_n}$ are exactly the same as $q_{\mathbf{d}}^{\mathbf{d}'}$'s, though the fluctuations of the field working as driving forces in the equations of motion have various frequencies.

In the one-detector case, when the natural frequency of the free detector Ω_0 comes close to the frequency of a free field mode, they mix and split into two dominant eigen-frequencies, a phenomenon similar to the anti-crossing of energy levels in atomic systems. These two neighboring eigen-modes produce the beats in the evolution of a mode function. In the weak coupling limit, the beat frequency is determined by the separation of these two neighboring eigen-frequencies and proportional to the square root of the coupling strength γ. The beats enjoy the largest time scale $O(\gamma^{-1/2})$ in the evolution of the mode functions in our compact space $\mathbf{S}^1$, which is quite different from the largest time scale $O(\gamma^{-1})$ for the detectors in Minkowski space.

When Ω_0 is not close to any frequency of the field modes, there may not be significant beats. However, if Ω_0 is located around, but not exactly at the middle point of two free field mode in the spectrum, these frequencies may mix and split into three dominant eigen-modes, which may produce the beats at a very large time scale. When this happens the beat frequency will be about the difference of the frequency difference between the higher and middle eigen-modes, and the frequency difference between the middle and the lower eigen-modes.

In the cases with two identical UD' detectors, there will be at least two dominant eigen-frequencies and so the mode functions always have significant beats, even when Ω_0 is not close to any frequency of the field modes. The beat frequency ranges from 2γ to $\sqrt{\gamma/\pi}$ in the weak coupling limit.

The beating behavior of the mode functions in turn affects the behavior of the correlators. In the one-detector case, the detector-field entanglement characterized by the value of the linear entropy, which is a function of the two-point correlators for the Gaussian states, gets the same beating features. This may be interpreted as periodic recoherence. In the two-detector case, entanglement dynamics between the two detectors also exhibit the same beating feature as in the mode functions. With a suitable choice of the parameter values one can observe a sequence of sudden-death and revival of quantum entanglement with a (beat) frequency one (twisted field) or two times (untwisted) of the beat frequency of the detector-detector mode functions. The beats at large time scale and the resonances around $t = nL$ distinguish the dynamics of a detector-field system in $\mathbf{S}^1 \times \mathbf{R}_1$ from the dissipative behavior of the same system living in Minkowski space $\mathbf{R}_1^1$.

5.3 Discreteness of field spectrum

Around the source point, the retarded Green's function of a field in Minkowski space looks the same as the one in any locally flat spacetime of the same dimension. Thus in a classical theory, if we couple a source such as a detector with the field in a very short duration, the classical physics around the interaction region in two different locally-flat spacetimes will be identical. In a quantum theory, however, different field spectra give different Wightman functions and produce different vacuum fluctuations. In particular, the field spectrum in a non-compact space is continuous, while the one in a compact space or in a cavity is discrete.

These differences originating from nontrivial topology or the existence of boundaries can affect the dynamics even for a single detector [4–6, 13]. A comparison of our early-time results for a single detector in the Einstein cylinder with the ones in Minkowski space is given in appendix A, where one can see that, while the evolution of the linear entropy of a detector in the twisted or untwisted field in the Einstein cylinder looks roughly the same as the one in Minkowski space at very early times, in most of the cases studied the difference becomes significant as the time scale becomes comparable to the crossing time of the compact spatial dimension for the retarded field. In those cases where the natural frequency of the detector is in resonance with the frequency of the untwisted field, this deviation emerges even earlier, as the evolution curve oscillates about the curve for the Minkowski case with a finite amplitude.

The discreteness of the field spectrum affects not only the self correlators of a single detector, corresponding to the detector-field entanglement, but also the cross correlators, which is important in the detector-detector entanglement. Our nonperturbative results indicate that early-time evolutions of quantum entanglement between two detectors in $\mathbf{S}^1 \times \mathbf{R}_1$ and in $\mathbf{R}_1^1$ is small. This is the range where perturbation theory results is expected to hold, as shown in ref. [13] in (3+1) dimensions. In our setup the discrepancy between the early-time results for the EnLC of a detector pair in 1) the twisted and 2) untwisted fields is more pronounced than the discrepancy between the linear entropies S_L of each single detector in these two fields. This may be due to the big contrast that the v-parts of the cross correlators of the detectors vanish in the twisted field but not in the untwisted field.

We end with a comment on the validity of time-dependent perturbation theory applied to entanglement problems in spacetimes with nontrivial topology and boundaries, such as studied here. In Minkowski space, TDPT with finite duration could be valid for the interaction time up to $O(1/\gamma)$. In $\mathbf{S}^1 \times \mathbf{R}_1$, by counting the exponent of the coupling, we can see that the effect of echoes comes from higher-order contributions (e.g., the λ^2 terms in eq. (3.1)). Nevertheless, our results indicate that even the first echo can have significant effect during $L < t < 2L$. So we know that as early as $t \approx L$ when the first echo returns, the lowest order perturbation result may become unreliable (figure 10). One needs to be careful, however, when comparing with the results of [13] which uses perturbation theory in (3+1) dimensions with only one spatial dimension being compact. The absence of echoes in the results [13] could be an intrinsic limitation of perturbation theory with a finite width of the Gaussian switching function, or that the echo effect is diluted by the other two non-compact dimensions. These points are worthy of further investigations by practitioners of perturbative switching methods.

Acknowledgments

A Detector in (1+1)D Minkowski space

For a single UD' detector at rest in (1+1)D Minkowski space, described by the action (2.2) and (2.3), initially in its ground state and coupled with the Minkowski vacuum of a massless scalar field at $t = 0$, the two-point correlators of the detector read

$$\langle \hat{Q}^2(t) \rangle = \langle \hat{Q}^2(t) \rangle_{\mathrm{a}} + \langle \hat{Q}^2(t) \rangle_{\mathrm{v}}, \qquad \langle \hat{P}^2(t) \rangle = \langle \hat{P}^2(t) \rangle_{\mathrm{a}} + \langle \hat{P}^2(t) \rangle_{\mathrm{v}} \tag{A.1}$$

with

$$\langle \hat{Q}^2(t) \rangle_{\mathrm{a}} = \frac{\hbar e^{-2\gamma t}}{2\Omega_0 \Omega^2} \left[\Omega_0^2 + \gamma(\Omega \sin 2\Omega t - \gamma \cos 2\Omega t) \right], \tag{A.2}$$

$$\langle \hat{Q}^2(t) \rangle_{\mathrm{v}} = \frac{2\hbar\gamma}{\pi\Omega^2} \Big\{ \mathcal{I}_1 \big[\Omega^2 + e^{-2\gamma t}(\Omega \cos \Omega t + \gamma \sin \Omega t)^2 \big] + \mathcal{I}_3 e^{-2\gamma t} \sin^2 \Omega t$$
$$- 2\Omega e^{-\gamma t} \big[\mathcal{S}_2(t) \sin \Omega t + \mathcal{C}_1(t)(\Omega \cos \Omega t + \gamma \sin \Omega t) \big] \Big\}, \tag{A.3}$$

$$\langle \hat{P}^2(t) \rangle_{\mathrm{a}} = \frac{\hbar\Omega_0}{2\Omega^2} e^{-2\gamma t} \left[\Omega_0^2 - \gamma(\Omega \sin 2\Omega t + \gamma \cos 2\Omega t) \right], \tag{A.4}$$

$$\langle \hat{P}^2(t) \rangle_{\mathrm{v}} = \frac{2\hbar\gamma}{\pi\Omega^2} \Big\{ \mathcal{I}_3 \big[\Omega^2 + e^{-2\gamma t}(\Omega \cos \Omega t - \gamma \sin \Omega t)^2 \big] + \mathcal{I}_1 e^{-2\gamma t} \Omega_0^4 \sin^2 \Omega t$$
$$- 2\Omega e^{-\gamma t} \big[\mathcal{S}_2(t)\Omega_0^2 \sin \Omega t + \mathcal{C}_3(t)(\Omega \cos \Omega t - \gamma \sin \Omega t) \big] \Big\}, \tag{A.5}$$

and $\langle \hat{Q}(t), \hat{P}(t) \rangle = \partial_t \langle \hat{Q}^2(t) \rangle / 2$. Here $\gamma \equiv \lambda^2/4$, $\Omega \equiv \sqrt{\Omega_0^2 - \gamma^2}$, and

$$\begin{aligned}
\mathcal{C}_{2n+1}(t) &\equiv \int_0^{\omega_M} \frac{\omega^{2n+1} \cos \omega t\, d\omega}{|(\gamma + i\omega)^2 + \Omega^2|^2} \\
&\overset{\omega_M \to \infty}{\longrightarrow} \mathrm{Re}\, \frac{i(\Omega + i\gamma)^{2n}}{4\gamma\Omega} \big\{ \cos T \big[\mathrm{Ci}(-T) + \mathrm{Ci}(T) \big] + 2 \sin T \, \mathrm{Si}(T) \big\},
\end{aligned} \tag{A.6}$$

$$\begin{aligned}
\mathcal{S}_{2n}(t) &\equiv \int_0^{\omega_M} \frac{\omega^{2n} \sin \omega t\, d\omega}{|(\gamma + i\omega)^2 + \Omega^2|^2} \\
&\overset{\omega_M \to \infty}{\longrightarrow} \mathrm{Re}\, \frac{i(\Omega + i\gamma)^{2n-1}}{4\gamma\Omega} \big\{ \sin T \big[\mathrm{Ci}(-T) + \mathrm{Ci}(T) \big] - 2 \cos T \, \mathrm{Si}(T) \big\},
\end{aligned} \tag{A.7}$$

$$\begin{aligned}
\mathcal{I}_1 &\equiv \int_0^{\omega_M} \frac{\omega\, d\omega}{|(\gamma + i\omega)^2 + \Omega^2|^2} \\
&\overset{\omega_M \to \infty}{\longrightarrow} \frac{1}{4\gamma\Omega} \left[\tan^{-1} \frac{\Omega^2 - \gamma^2}{2\gamma\Omega} + \frac{\pi}{2} \right] = \frac{i}{4\gamma\Omega} \ln \frac{\gamma - i\Omega}{\gamma + i\Omega},
\end{aligned} \tag{A.8}$$

$$\mathcal{I}_3 \equiv \int_0^{\omega_M} \frac{\omega^3\, d\omega}{|(\gamma + i\omega)^2 + \Omega^2|^2} \approx (\Omega^2 - \gamma^2)\mathcal{I}_1 + \ln \frac{\omega_M}{\Omega_0} \tag{A.9}$$

for $\omega_M \gg \Omega$, with $n = 0, 1, 2, \ldots$, $T \equiv (\Omega + i\gamma)t$, the sine (cosine) integral function Si (Ci), the Euler's constant γ_e, and the UV cutoff ω_M. All the above two-point correlators of the detector depend on $\mathcal{I}_3$, and so all explicitly depend on the UV cutoff. At late times ($t \gg 1/\gamma$), one has $\langle \hat{Q}, \hat{P} \rangle \to 0$ and $\langle \hat{Q}^2 \rangle \to 2\hbar\gamma\mathcal{I}_1/\pi$, but $\langle \hat{P}^2 \rangle \to 2\hbar\gamma\mathcal{I}_3/\pi$ is still cutoff dependent significantly.

The above results are actually identical to the two-point correlators of a UD detector in (3+1) dimensional Minkowski space [30]. To see this, one may insert $\omega_M = 2\pi\Omega e^{\Lambda_1 + \gamma_e}$ to the $\mathcal{I}_3\Omega^2$ term in $\langle \hat{P}^2(t) \rangle_{\rm v}$, while substitute $\omega_M = 2\pi\Omega e^{\Lambda_0 + \gamma_e}$ to other $\mathcal{I}_3$'s. Thus we can borrow the interpretation from ref. [30] that the constant Λ_1 corresponds to the time-resolution of the detector, and the constant Λ_0 corresponds to the time scale of switching-on the interaction at the initial moment.

We have also found that, for the interaction action S'_I in (2.7), the correlator $\langle \hat{P}'^2 \rangle$ with physically non-measurable momentum $P' = \partial_t Q + \lambda \Phi_{x=0}$ is both IR and UV divergent.

In $S^1 \times R_1$, the correlators of a single detector at early times before the first echo returns can also be expressed as eqs. (A.2)–(A.5) from (3.3) and (3.4), with the integrals in eqs. (A.6) to (A.9) reduced to the the Riemann sums of the integrands: $\int_0^{\omega_{\max}} \to \sum_{n=1}^{n_{\max}}$, $\omega \to \omega_n = 2n\pi/L$, $n = 1, 2, 3, \ldots$, and $d\omega \to \Delta\omega \equiv \omega_{n+1} - \omega_n = 2\pi/L$. In addition, for the cases with the untwisted field, one needs to include the zero-mode contribution from (3.5). While the difference between each integral of (A.6)–(A.9) in R_1^1 and the corresponding discrete sum in $S^1 \times R_1$ can be large, most of the differences turn out to cancel in the correlators. The difference between the correlators with discrete and continuous spectra can be minimized by fine-tuning the parameters corresponding to the UV cutoff (Λ_0 and Λ_1) in the R_1^1 case. We find that the correlators and S_L in $S^1 \times R_1$ will not deviate from those in R_1^1 significantly until a time scale comparable to L.

In figure 13 we demonstrate some examples of the early-time behavior of the linear entropy S_L for a UD' detector initially in its ground state. In each plot, the averaged decaying behavior of the three curves at a time scale of $O(L)$ are very similar, while the untwisted field usually gives a greater oscillation at a frequency $\approx 2\Omega$ about a fine-tuned curve for the R_1^1 case than the twisted field does. These oscillations are more significant for large L ($L \gg 2\pi/\Omega$, upper right), and the most significant on resonance ($\Omega \approx 2\pi n/L$ with integer n, lower row). Fortunately, the amplitudes of such oscillations are always bounded and will saturate when $t \sim O(1/\gamma)$, provided that t is still not very close to L. To check this in the on-resonance cases, in the lower-right plot of figure 13, we show the frequency dependence of the S_L curve with the untwisted field subtracted by the one with the twisted field at a fixed time (at each frequency one has some fine-tuned S_L evolution curves in the $\mathbf{R}_1^1$ case between the untwisted and twisted results). Indeed, one can see that, around the resonance peaks, the amplitude of the oscillation at a resonant frequency is not very far from those at the neighboring frequencies in value.

When approaching $t = L$, in contrast to the curves for the R_1^1 cases, the curves for the detectors in the untwisted and twisted fields in $\mathbf{S}^1 \times \mathbf{R}_1$ get large but opposite resonant behaviors in time, which have the same origin as those spikes around $t = nL$ in figures 6–12.

The evolution curves for the probability of finding the same detector in the first excited state, $\rho_{1,1}^R$, look very similar to the ones in figure 13. $\rho_{1,1}^R$ here can be interpreted as the
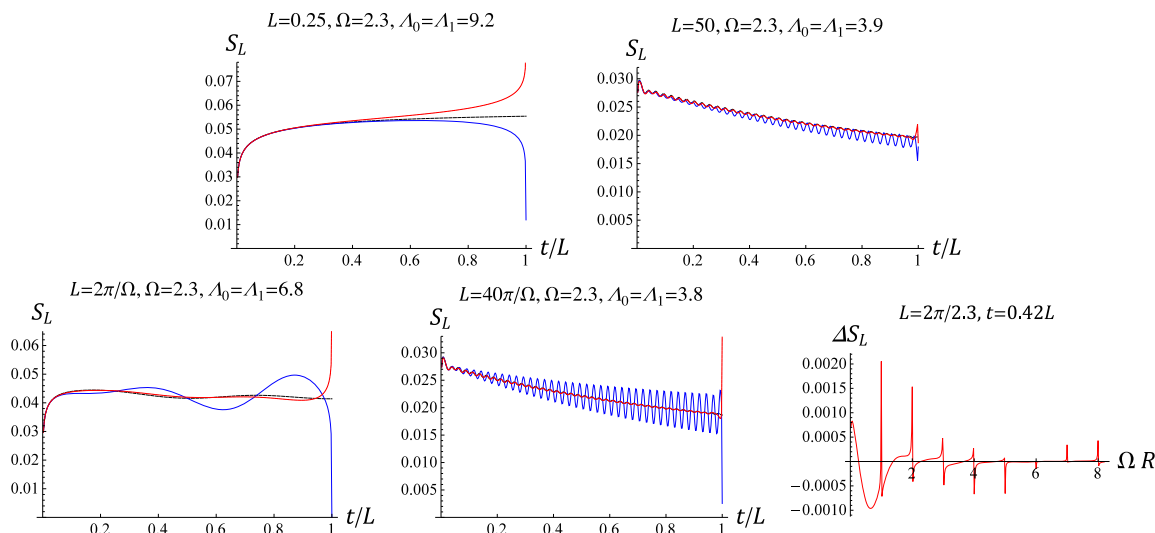
Figure 13. Early-time linear entropy S_L of a UD' detector initially in its ground state and coupled to the untwisted (blue) and twisted (red dotted) fields in $\mathbf{S}^1 \times \mathbf{R}_1$ at $t = 0$, compared with the one in $\mathbf{R}_1^1$ (black dashed). Here $\gamma = 0.01$ and $n_{\max} = 10000$. The natural period of the harmonic oscillator is $2\pi/\Omega \approx 2.732$ in these plots. (Lower right) Frequency dependence of $\Delta S_L \equiv S_L|_{\text{untwisted}} - S_L|_{\text{twisted}}$, which is the difference of S_L between the linear entropies in the untwisted and the twisted fields at a fixed time $t = 0.42L$. There are spikes around $\Omega = n/R = 2n\pi/L$, $n = 1, 2, 3, \ldots$.

transition probability from the initial ground state of the detector to the first excited state in TDPT [30]. We find the values of $\rho_{1,1}^R(t)$ in most of the history in $0 < t < L$ are about $O(\gamma)$, indicating that one should be able to see some hints of the non-perturbative $\rho_{1,1}^R(t)$ curves in the leading order ($\sim \gamma^1$) of the perturbation theory with a finite duration (cf. figure 10).

Open Access. This article is distributed under the terms of the Creative Commons Attribution License ([CC-BY 4.0](https://creativecommons.org/licenses/by/4.0/)), which permits any use, distribution and reproduction in any medium, provided the original author(s) and source are credited.

References

[1] *International Society for Relativistic Quantum Information*, www.isrqi.net.

[2] S.-Y. Lin, C.-H. Chou and B.L. Hu, *Disentanglement of two harmonic oscillators in relativistic motion*, *Phys. Rev.* **D 78** (2008) 125025 [arXiv:0803.3995] [INSPIRE].

[3] S.-Y. Lin, C.-H. Chou and B.L. Hu, *Quantum teleportation between moving detectors*, *Phys. Rev.* **D 91** (2015) 084063 [arXiv:1502.03539] [INSPIRE].

[4] P. Langlois, *Causal particle detectors and topology*, *Annals Phys.* **321** (2006) 2027 [gr-qc/0510049] [INSPIRE].

[5] P. Langlois, *Imprints of spacetime topology in the Hawking-Unruh effect*, Ph.D. Thesis, University of Nottingham (2005) [gr-qc/0510127] [INSPIRE].

[6] R. Zhou, R.O. Behunin, S.-Y. Lin and B.L. Hu, *Boundary effects on quantum entanglement and its dynamics in a detector-field system*, *JHEP* **08** (2013) 040 [arXiv:1301.0073] [iNSPIRE].

[7] T.H. Boyle, *Casimir forces and boundary conditions in one dimension: attraction, repulsion, Planck spectrum, and entropy*, *Am. J. Phys.* **71** (2003) 990 [quant-ph/0211109].

[8] T. Aoki et al., *Observation of strong coupling between one atom and a monolithic microresonator*, *Nature* **443** (2006) 671 [quant-ph/0606033].

[9] C.J. Isham, *Twisted quantum fields in a curved space-time*, *Proc. Roy. Soc. Lond.* **A 362** (1978) 383.

[10] S.J. Avis and C.J. Isham, *Vacuum solutions for a twisted scalar field*, *Proc. Roy. Soc. Lond.* **A 363** (1978) 581.

[11] J.S. Dowker and R. Banach, *Quantum field theory on Clifford-Klein space-times. The effective Lagrangian and vacuum stress energy tensor*, *J. Phys.* **A 11** (1978) 2255 [iNSPIRE].

[12] B.S. DeWitt, C.F. Hart and C.J. Isham, *Topology and quantum field theory*, *Physica* **A 96** (1979) 197 [iNSPIRE].

[13] E. Martín-Martínez, A.R.H. Smith and D.R. Terno, *Spacetime structure and vacuum entanglement*, *Phys. Rev.* **D 93** (2016) 044001 [arXiv:1507.02688] [iNSPIRE].

[14] I. Bengtsson and K. Życzkowski, *Geometry of quantum states: an introduction to quantum entanglement*, Cambridge University Press, Cambridge U.K. (2006).

[15] D. Zhou, G.W. Chern, J. Fei and R. Joynt, *Topology of entanglement evolution of two qubits*, *Int. J. Mod. Phys.* **B 26** (2012) 1250054 [arXiv:1007.1749].

[16] N.T.T. Nguyen and R. Joynt, *Topology of quantum discord*, arXiv:1310.5286.

[17] S.-Y. Lin and B.L. Hu, *Temporal and spatial dependence of quantum entanglement from a field theory perspective*, *Phys. Rev.* **D 79** (2009) 085020 [arXiv:0812.4391] [iNSPIRE].

[18] M. Kac, *Some remarks on the use of probability in classical statistical mechanics*, *Acad. Roy. Belg. Bull. Cl. Sci.* **42** (1956) 356.

[19] J.M. Oberreuter, I. Homrighausen and S. Kehrein, *Entanglement propagation and typicality of measurements in the quantum Kac ring*, *Annals Phys.* **348** (2014) 324 [arXiv:1312.1726].

[20] W.G. Unruh, *Notes on black hole evaporation*, *Phys. Rev.* **D 14** (1976) 870 [iNSPIRE].

[21] B.S. DeWitt, *Quantum gravity: the new synthesis*, in *General relativity: an Einstein centenary survey*, S.W. Hawking and W. Israel eds., Cambridge University Press, Cambridge U.K. (1979).

[22] W.G. Unruh and W.H. Zurek, *Reduction of a wave packet in quantum Brownian motion*, *Phys. Rev.* **D 40** (1989) 1071 [iNSPIRE].

[23] D.J. Raine, D.W. Sciama and P.G. Grove, *Does a uniformly accelerated quantum oscillator radiate?*, *Proc. Roy. Soc. Lond.* **A 435** (1991) 205.

[24] A. Raval, B.L. Hu and J. Anglin, *Stochastic theory of accelerated detectors in a quantum field*, *Phys. Rev.* **D 53** (1996) 7003 [gr-qc/9510002] [iNSPIRE].

[25] B.L. Hu and A. Raval, *Is there emitted radiation in Unruh effect?*, quant-ph/0012134 [iNSPIRE].

[26] J. Louko, *Unruh-DeWitt detector response across a Rindler firewall is finite*, *JHEP* **09** (2014) 142 [arXiv:1407.6299] [InSPIRE].

[27] E. Martín-Martínez and J. Louko, *Particle detectors and the zero mode of a quantum field*, *Phys. Rev.* **D 90** (2014) 024015 [arXiv:1404.5621] [InSPIRE].

[28] S.-Y. Lin and B.L. Hu, *Accelerated detector-quantum field correlations: from vacuum fluctuations to radiation flux*, *Phys. Rev.* **D 73** (2006) 124018 [gr-qc/0507054] [InSPIRE].

[29] N.D. Birrell and P.C.W. Davies, *Quantum fields in curved space*, Cambridge University Press, Cambridge U.K. (1982) [InSPIRE].

[30] S.-Y. Lin and B.L. Hu, *Backreaction and the Unruh effect: new insights from exact solutions of uniformly accelerated detectors*, *Phys. Rev.* **D 76** (2007) 064008 [gr-qc/0611062] [InSPIRE].

[31] G. Vidal and R.F. Werner, *Computable measure of entanglement*, *Phys. Rev.* **A 65** (2002) 032314 [InSPIRE].

[32] M.B. Plenio, *Logarithmic negativity: a full entanglement monotone that is not convex*, *Phys. Rev. Lett.* **95** (2005) 090503 [*Erratum ibid.* **95** (2005) 119902] [quant-ph/0505071].

[33] A. Mari and D. Vitali, *Optimal fidelity of teleportation of coherent states and entanglement*, *Phys. Rev.* **A 78** (2008) 062340 [arXiv:0808.2829].